Drug Resistance Updates 67 (2023) 100914

Contents lists available at ScienceDirect

Drug Resistance Updates

journal homepage: www.elsevier.com/locate/drup

Acquired non-thermal plasma resistance mediates a shift towards aerobic glycolysis and ferroptotic cell death in melanoma

Abraham Lin [a,b,*], Maxime Sahun [a], Eline Biscop [a,b], Hanne Verswyvel [a,b], Jorrit De Waele [b], Joey De Backer [c], Claudia Theys [c], Bart Cuypers [d], Kris Laukens [d], Wim Vanden Berghe [c], Evelien Smits [b,1], Annemie Bogaerts [a,1]

[a] Plasma Lab for Applications in Sustainability and Medicine-ANTwerp (PLASMANT), University of Antwerp, Antwerp-Wilrijk, Belgium
[b] Center for Oncological Research (CORE), Integrated Personalized and Precision Oncology Network (IPPON), University of Antwerp, Antwerp-Wilrijk, Belgium
[c] Protein Chemistry, Proteomics, and Epigenetic Signalling, University of Antwerp, Antwerp-Wilrijk, Belgium
[d] Adrem Data Lab, University of Antwerp, Antwerp, Belgium

ARTICLE INFO

Keywords:
Non-thermal plasma
Cancer treatment
Melanoma
Resistance
Plasma sensitivity
Metabolism
Aerobic glycolysis
Ferroptosis
Lipid peroxidation

ABSTRACT

Aims: To gain insights into the underlying mechanisms of NTP therapy sensitivity and resistance, using the first-ever NTP-resistant cell line derived from sensitive melanoma cells (A375).

Methods: Melanoma cells were exposed to NTP and re-cultured for 12 consecutive weeks before evaluation against the parental control cells. Whole transcriptome sequencing analysis was performed to identify differentially expressed genes and enriched molecular pathways. Glucose uptake, extracellular lactate, media acidification, and mitochondrial respiration was analyzed to determine metabolic changes. Cell death inhibitors were used to assess the NTP-induced cell death mechanisms, and apoptosis and ferroptosis was further validated via Annexin V, Caspase 3/7, and lipid peroxidation analysis.

Results: Cells continuously exposed to NTP became 10 times more resistant to NTP compared to the parental cell line of the same passage, based on their half-maximal inhibitory concentration (IC50). Sequencing and metabolic analysis indicated that NTP-resistant cells had a preference towards aerobic glycolysis, while cell death analysis revealed that NTP-resistant cells exhibited less apoptosis but were more vulnerable to lipid peroxidation and ferroptosis.

Conclusions: A preference towards aerobic glycolysis and ferroptotic cell death are key physiological changes in NTP-resistance cells, which opens new avenues for further, in-depth research into other cancer types.

Introduction

Non-thermal plasma (NTP), ionized gas generated near room temperature and at atmospheric pressure, has been investigated for several biomedical applications throughout the decade, but in recent years, there has been an increased focus on cancer immunotherapeutic applications (Khalili et al., 2019; Dubuc et al., 2018; Keidar et al., 2018). Preclinical research has demonstrated that NTP induces immunogenic cell death (ICD) in various cancer types and several studies have even reported abscopal effects in vivo (Lin et al., 2022; Mahdikia et al., 2021; Chen et al., 2020). While NTP application exposes cells and tissue to a variety of physical (e.g. high electric fields, ultraviolet light) and chemical components (e.g. various radical species and neutral molecules), several studies have demonstrated that the NTP-generated short-lived reactive oxygen species (ROS), particularly •OH, •NO, and O/O_3, are the main effectors of cancer cell death, including ICD (Bekeschus et al., 2017; Lin et al., 2017, 2019; Wende et al., 2019; Bekeschus et al., 2020). In this sense, NTP is similar to other redox therapies, in which localized delivery of ROS can induce confined tumor cell destruction, while stimulating anti-cancer immunity, modulating damage to healthy tissue, and reducing harmful adverse effects.

Cancer-related NTP applications in the clinical setting have only just started, and no immediate or late adverse effects have been reported. New clinical trials are also now in preparation. Friedman et al. (2017) treated patients with pre-cancerous skin lesions, actinic keratosis, and reported that 12 of 17 lesions were fully resolved or significantly

* Corresponding author at: Plasma Lab for Applications in Sustainability and Medicine-ANTwerp (PLASMANT), University of Antwerp, Antwerp-Wilrijk, Belgium.
E-mail address: abraham.lin@uantwerpen.be (A. Lin).
[1] Shared senior authors

https://doi.org/10.1016/j.drup.2022.100914
Received 7 November 2022; Received in revised form 15 December 2022; Accepted 23 December 2022
Available online 29 December 2022

improved after 1 round of NTP treatment in a 1-month follow-up. Metelmann et al. treated patients with locally advanced squamous cell carcinoma with NTP for palliation. Not only did NTP treatment reduce the need for pain medication and ease the odor of infected tumor ulcers, but partial remission was observed in 2 patients (Metelmann et al., 2018). Unfortunately, after 7 months, treatment began to fail for 1 of the patients. These reports highlight the importance of understanding cancer sensitivity to NTP, as well as the potential for acquired resistance, which remains a dire clinical issue in oncology. Hence, this will be particularly critical as more clinical trials with NTP therapy are set up and carried out.

In this study, we developed, for the first time, an NTP-resistant melanoma cell line, through repeat exposure to NTP, as a model to investigate NTP sensitivity and resistance pathways. After 12 consecutive weeks of NTP exposure, the NTP-resistant cell line was nearly 10 times more resistant to NTP compared to the parental cell line of the same passage, based on their half-maximal inhibitory concentration (IC_{50}). Whole transcriptome sequencing (RNAseq) was performed on both the NTP-resistant and parental cell lines, which revealed several differentially expressed genes (DEG). Gene set enrichment analysis revealed that the NTP-resistant cell line had altered metabolic pathways compared to the parental. Interestingly, the hypoxic gene signature was significantly upregulated in the NTP-resistant cells, despite culturing in normoxic conditions. Therefore, we hypothesized that NTP-resistant cells were more prone to aerobic glycolysis, which was further evidenced via functional assessment. Evaluation of the response to NTP revealed that the parental cell line demonstrated higher upregulation of apoptosis compared to NTP-resistant cells. Interestingly, although NTP-resistant cells were less apoptotic compared to their parental counterparts, they were also more prone to lipid peroxidation and potentially ferroptosis. We also attempted to further evaluate NTP-resistance in a more advanced 3D spheroid model, and measured distinct differences in spheroid phenotype. Therefore, besides the identification of several critical physiological changes in cells that have developed NTP-resistance, we have developed — for the first time — a valuable model for studying fundamental NTP sensitivity and resistance mechanisms, which can be applied to other cell lines and cancer types. Altogether, these insights from our work can help inform on strategic combination strategies with existing cancer therapies and provide the first steps towards identifying potential treatment biomarkers for NTP therapy.

Results

Development and confirmation of acquired NTP resistance

An NTP-resistant cell line (A375-NTP-R) was developed from the parental malignant human melanoma cell line (A375) via weekly exposure to NTP (Fig. 1a). The microsecond-pulsed dielectric barrier discharge (DBD) NTP system was used, and treatment energy was increased every 2 weeks by increasing the pulse frequency by 100 Hz over a period of at least 12 weeks, starting at 100 Hz and up to 1000 Hz (1.8—18 J), while the parental A375 cell line was cultured and passaged in parallel. At the end of the 12-week period, the NTP-resistant and parental cell lines were characterized and compared to each other. Mycoplasma testing was performed to ensure that cells remained uncontaminated and short tandem repeat (STR) analysis authenticated the cell lines with their original A375 profile.

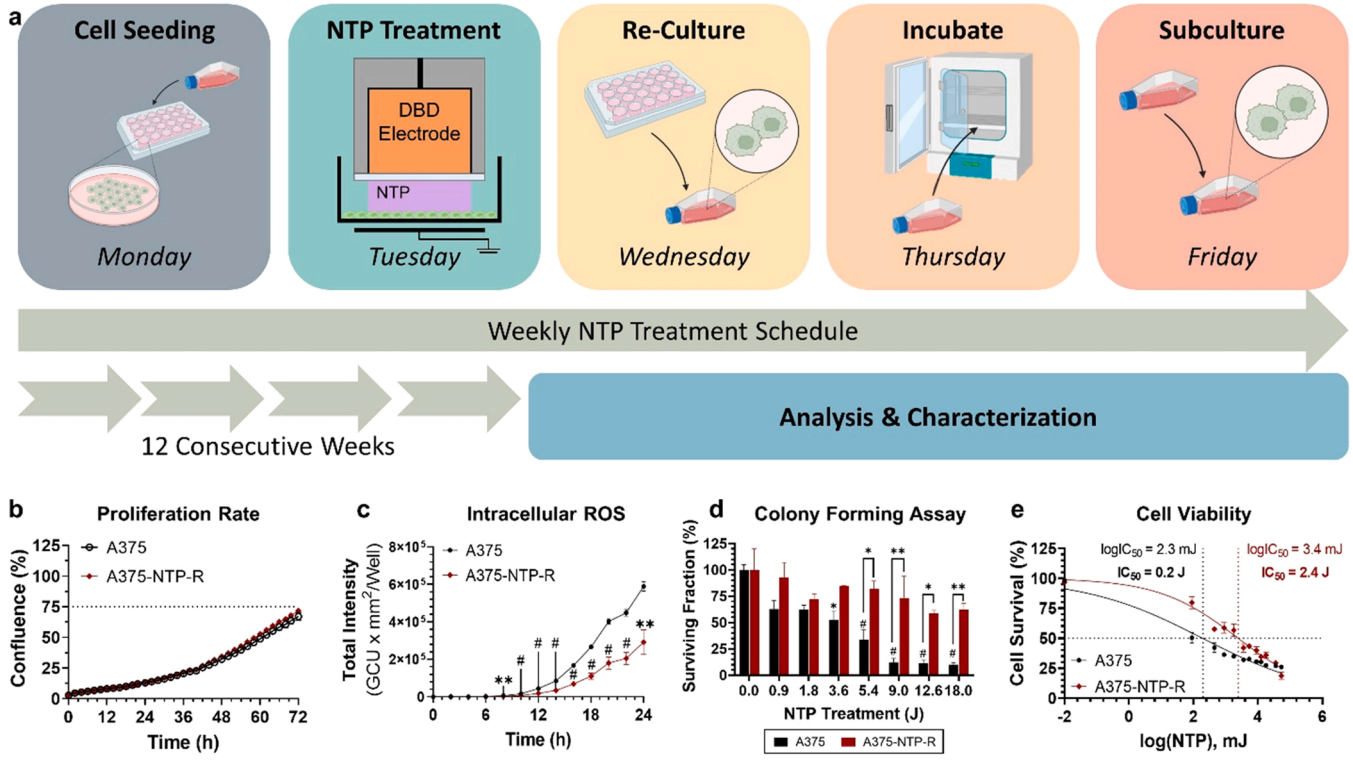

Fig. 1. Development of an NTP-resistant melanoma cell line. a The A375 cell line was repeatedly treated once per week, while the parental A375 cell line was cultured in parallel to maintain the same number of passages. Treatments and culturing were performed for a period of at least 12 weeks, consecutively, followed by analysis and characterization. In this manner, comparisons were made between the A375-NTP-R and the parental A375 cell lines at the same passage number. The baseline b proliferation rate and the c intracellular ROS levels were measured and compared for the NTP-resistant and parental cell lines. d The colony formation assay was performed, and the calculated survival fraction revealed an increased tolerance to NTP treatment in the A375-NTP-R cell line compared to the parental. Statistical significance was calculated via a two-way ANOVA with Tukey's multiple comparisons test. * $p \leq 0.05$, * * $p \leq 0.01$, # $p \leq 0.001$ (more detailed p values are reported in text). e Cell survival was determined with nuclear and cell death staining and was analyzed via image cytometry. From the nonlinear regression analysis, the IC_{50} value of the A375-NTP-R (2.4 J) was determined to be 10 times higher than that of the parental (0.2 J).

While no changes to cell morphology were visibly observed (Fig. S1), the baseline proliferation rate and intracellular ROS levels were measured using live-cell imaging to assess the effects of repeat NTP exposure on cell physiology. Based on their confluence, no differences in proliferation rate were observed (Fig. 1b). Real-time monitoring of the intracellular redox state was performed using a fluorogenic probe (CellROX® Green Reagent, Invitrogen™), which can permeate cell membranes and exhibits stable, green fluorescence upon oxidation by ROS. Interestingly, the A375-NTP-R cell line exhibited lower intracellular ROS at 8 h following incubation (p=0.002), which persisted for at least 24 h (Fig. 1c).

NTP-resistance was confirmed with the colony formation assay (CFA) and the image cytometry cell survival assay. Based on the CFA, the survival fraction of the parental A375 cells was significantly reduced at 3.6 J treatment energy (52 ± 8%; p=0.015) compared to untreated, while the survival fraction of the A375-NTP-R remained clearly above 50%, even at the highest treatment energy of 18.0 J (62 ± 6%) (Fig. 1d). Moreover, the surviving fractions of the resistant and parental cell lines were statistically different at treatment energy above 3.6 J, which further indicated that the A375-NTP-R cells have become more tolerant of NTP treatment.

Cell viability was assessed 24 h post NTP treatment by dual-staining with a nuclear dye and a cell death stain, and analysis was performed with image cytometry. Cell survival was calculated based on the total number of live cells per well, normalized to the untreated. Both cell lines demonstrated a dose-dependent reduction in cell survival following NTP treatment (Fig. 1e). However, the NTP energy required to induce 50% cell death (IC_{50}) was 10 times higher for the resistant A375-NTP-R cell line (IC_{50}=2.4 J; 95% confidence interval: 1.8–3.2 J) compared to the parental cell line (IC_{50}=0.23 J; 95% confidence interval: 0.1–0.3 J). Therefore, taken together, these results strongly indicate that the melanoma cells were able to acquire resistance to NTP treatment following prolonged and recurrent exposure.

Characterization of sensitive and resistant cell lines at baseline

In order to determine the changes to the A375-NTP-R cell line following repeat NTP exposure, we compared the whole transcriptome of the resistant cell line with that of the parental A375 cell line. DEG analysis with edgeR revealed 51 genes that were significantly up- or downregulated (q≤0.05) when comparing the resistant cell line to the parental (Fig. 2a). The top 3 highest DEG were *CXCL8* (Log_2FC=1.965, q=0.02), *HDAC11* (Log_2FC=1.952, q=0.04), and *SOX11* (Log_2FC=1.736, q≤0.0001). Interestingly, *CXCL8*, the gene which encodes for the chemokine interleukin 8 (IL-8), has been reported to be a predominant stimulator of tumor growth, angiogenesis, and metastasis in melanoma, and overexpression of *CXCL8* can be in response to chemotherapeutic intervention or environmental stresses, such as hypoxia (Liu et al., 2016). Moreover, *CXCL8* has been linked to the evasion of programmed cell death. HDACs, on the other hand, are enzymes that catalyze the removal of acetyl functional groups from proteins, leading to epigenetic modifications (Seto and Yoshida, 2014). *HDAC11* has also recently been identified as a novel mitochondrial regulator of fatty acid oxidative metabolism and glycolysis (Hurtado et al., 2021; Bi et al., 2021; Fan et al., 2018). This could have profound effects on the regulation and control of various metabolic cell death processes. Finally, *SOX11* is a transcription factor that normally regulates progenitor and stem cell behavior, and has also been linked to cancer progression (Tsang et al.). Therefore, these key genes for chemokines (*CXCL8*), enzymes (*HDAC11*), and transcription factors (*SOX11*) could be linked to the observed NTP resistance in the A375-NTP-R cell line.

Using 2-way hierarchical clustering, the top 150 genes were grouped into 4 gene clusters based on their expression profile patterns (Fig. 2b), and functional annotations were prescribed by correlating annotation features from the Hallmark gene sets on the Molecular Signatures Database (v7.5.1). Here, the genes in the S4 cluster showed the highest correlation, including several immune signatures (interferon alpha response, IL2-STAT5 signaling), ROS signatures (peroxisome, ROS pathway), and the majority being metabolic signatures (glycolysis, xenobiotic metabolism, bile acid metabolism, fatty acid metabolism, oxidative phosphorylation, MTORC1 signaling, and hypoxia). Next, gene set enrichment analysis (GSEA) was performed using 2 well-defined and the most widely used gene sets: the KEGG (Kanehisa and Goto, 2000) and Hallmark gene sets (Liberzon et al., 2015). With the KEGG Pathway gene set, 6 pathways were significantly upregulated (q≤0.05) (Fig. 2c). Interestingly, all 6 pathways were associated with metabolic processes, indicating that the A375-NTP-R cells may have undergone metabolic rewiring. From the Hallmark gene set, only the hypoxia pathway surpassed the significance threshold (q=0.012) and demonstrated a normalized enrichment score (NES) of 1.494. This was particularly striking, as our NTP-resistant cells were cultured in normoxic conditions (95% air and 5% CO_2). However, a hypoxic signature is also associated with metabolic rewiring, similar to the Warburg effect, where glycolysis is favored as the major cellular energy process, even in the presence of oxygen (Bartrons and Caro, 2007). While the glycolysis gene set did not meet our false discovery rate threshold, it is worth noting that it appears slightly enriched (NES=1.257, q=0.1229), and nearly no change in oxidative phosphorylation was observed (NES=1.187, q=0.5282) (Fig. S2).

Taken together, the RNAseq analysis appeared to indicate that a major difference between the NTP-resistant and parental cells lies in their metabolic function, with the resistant cells potentially favoring more aerobic glycolysis. Therefore, in the subsequent experiments, we investigated several hallmarks of aerobic glycolysis and compared them between the NTP-resistant and parental cell lines.

Evaluation of metabolic shift and indicators of aerobic glycolysis

In order to further investigate the hypoxic signature and potential metabolic shift in the NTP-resistant cells, we analyzed the protein expression of two hypoxia markers: hypoxia-inducible factor 1-alpha (HIF-1α), a central regulator of the hypoxic response, and BLC2 interacting protein 3 (BNIP3), a downstream target gene. Western Blot analysis was performed on the parental and NTP-resistant cell lines, while a parental cell line cultured under hypoxic conditions (1% oxygen) was used as a positive control (A375-Hypoxia).

Based on the Western Blot (Fig. 3a), the HIF-1α and BNIP3 protein expression was quantified and normalized to the actin expression per sample (Fig. 3b). The A375-Hypoxia cells showed a 6.6-fold increase in HIF-1α (p≤0.0001) and a 3.8-fold increase in BNIP3 (p≤0.0001) compared to the parental A375. While the A375-NTP-R cell line did not demonstrate elevated protein levels to the extent of cells under hypoxic conditions, it also showed significantly elevated expressions for both HIF-1α (2.1 ± 0.3-fold; p=0.0119) and BNIP3 (1.9 ± 0.5-fold; p=0.0497) compared to the parental A375 (Fig. 3b). HIF-1α-driven BNIP3 has been reported to contribute to reduced cellular oxygen consumption, thus directing metabolic function towards low oxygen conditions (Vara-Pérez et al., 2021). Therefore, these data are in-line with our RNAseq analysis (Fig. 2), and metabolic rewiring towards aerobic glycolysis was further investigated.

Under normoxic and physioxic conditions, cellular metabolism undergoes mitochondrial oxidative phosphorylation respiration, to convert glucose energy resources into adenosine 5′-triphosphate (ATP), the energy molecule required for living cells. However, under hypoxic conditions, or during aerobic glycolysis, cellular metabolism favors lactic acid fermentation (Bartrons and Caro, 2007). While lactic acid fermentation produces ATP much faster than mitochondrial respiration, it is comparably a highly inefficient process, as only 2 ATP molecules are produced per glucose molecule, compared to 38 ATP molecules via aerobic respiration. Therefore, cells utilizing aerobic fermentation must take up higher amounts of glucose to keep up with cellular energy demands. As such, we first evaluated the glucose uptake level for the NTP-resistant

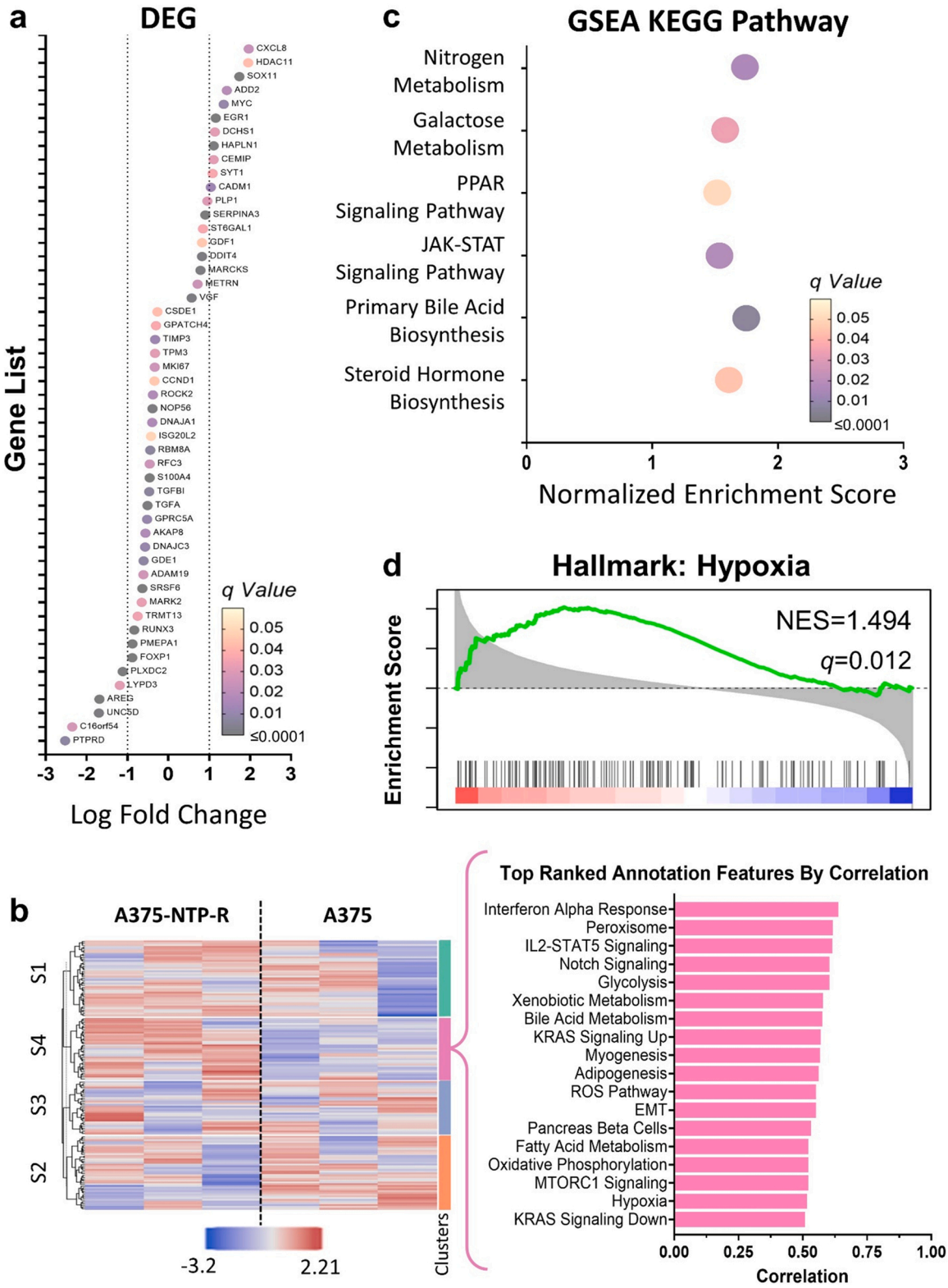

Fig. 2. Whole transcriptome analysis and characterization of A375 cells with acquired NTP resistance. a Differential gene expression (DEG) analysis, comparing the resistant cell line to the parental, using edgeR, revealed 51 genes that were significantly up- or downregulated ($q \leq 0.05$). b The top 150 genes from 2-way hierarchical clustering showed 4 clusters, with cluster S4 demonstrating the highest correlation with the annotation features from the Hallmark gene sets. Of these gene sets, the majority are associated with metabolic processes (glycolysis, xenobiotic metabolism, bile acid metabolism, fatty acid metabolism, oxidative phosphorylation, MTORC1 signaling, and hypoxia). GSEA analysis was performed using the c KEGG pathway and d Hallmark gene sets, both revealing significant enrichment of metabolic pathways. The green line indicates the enrichment profile, and the y-axis indicates the enrichment score based on the ranked list of genes.

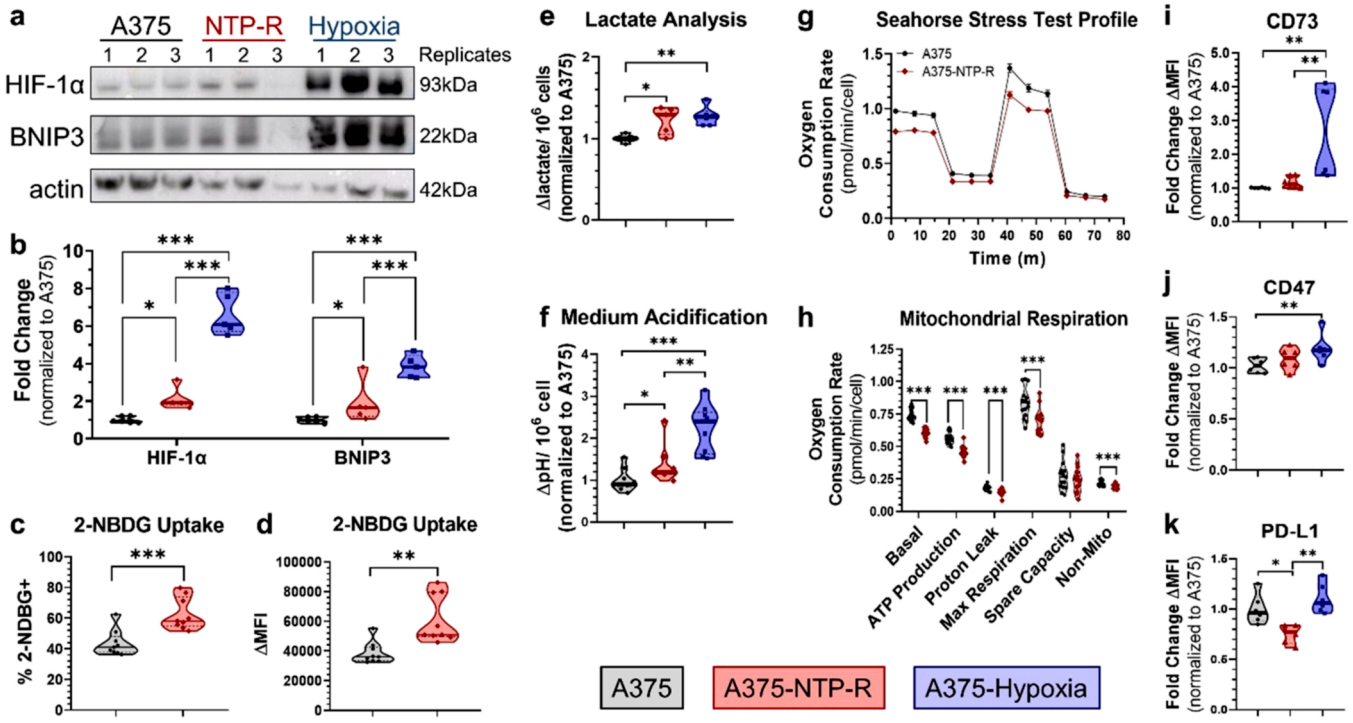

Fig. 3. The NTP-resistant cell line demonstrated metabolic rewiring towards more lactic acid fermentation. a Western Blotting of two hypoxia markers, HIF-1α and BNIP3, was performed for both the parental A375 cells and the NTP-resistant cells (NTP-R). The parental cells cultured under hypoxic conditions, 1% oxygen (A375-Hypoxia), were used as a positive control. b Quantification of the Western Blot relative to actin revealed that the NTP-resistant cells had increased expression of both HIF-1α and BNIP3, though not to the same extent as the A375-Hypoxia cells. Data are represented as fold change of the parental protein levels. Glucose uptake, assessed using the 2-NBDG fluorescent glucose analog, showed a c higher percentage of uptake and d amount of uptake in the NTP-resistant cells compared to the parental. Cell culture media were collected from the culture flasks with the different cell lines and assessed for e lactate concentration and f change in pH. The A375-NTP-R cells demonstrated a significant increase in both lactate secretion and medium acidification, compared to the parental A375, though not to the same degree as hypoxic cells. The Seahorse XF Cell Mito Stress assay was used to measure oxygen consumption rate as an indicator of mitochondrial fitness. Based on the g stress test profile, h mitochondrial respiration was evaluated, revealing that this was decreased for the A375-NTP-R cells, compared to the parental cells. The effect of metabolic shift on the immunogenicity of cancer cells was also evaluated by measuring the immunosuppressive signals i CD73, j CD47, and k PD-L1. Data here are represented as mean ± SEM and each biologically independent sample is shown. Statistical significance was calculated using the generalized linear mixed model. * $p \leq 0.05$, * * $p \leq 0.01$, * ** $p \leq 0.001$ (more detailed p values are reported in the text).

and parental cell line.

Both cell lines were cultured in 24-well plates with glucose-free media and a fluorescent glucose analog, 2-(N-(7-Nitrobenz-2-oxa-1,3-diazol-4-yl)Amino)− 2-Deoxyglucose (2-NBDG), was added to measure differential uptake by cells, using flow cytometry analysis (Fig. S3). Overton analysis, performed using unstained cells for each sample, revealed that a significantly higher percentage of A375-NTP-R cells had taken up 2-NBDG (62.6 ± 3.5%; $p \leq 0.0001$) compared to that of the parental A375 cells (43.6 ± 2.8%) (Fig. 3c). Furthermore, the mean fluorescence intensity, corrected against the unstained for each sample (ΔMFI), also revealed that the A375-NTP-R cells had a significantly higher amount of 2-NBDG uptake ($p=0.0207$) compared to that of parental cells (Fig. 3d). From these data, it appeared that the NTP-resistant cells have higher glucose uptake compared to the parental cells, for both the percentage of cells and the amount of glucose, as indicative of more aerobic glycolysis.

Another indicator of higher aerobic glycolysis metabolism is the release of lactate from the cell and the acidification of the extracellular environment. Therefore, following cell culture, the culture media were collected and lactate concentrations and pH were measured. The baseline lactate concentrations and pH of the media without cells (both in normoxia and hypoxia) were measured and did not show any significant difference (Fig. S4). Both lactate concentrations and pH were represented as the change from baseline and corrected for the number of cells in the flask. Both the A375-Hypoxia and the A375-NTP-R cells showed a significant increase in lactate concentration (1.27 ± 0.05-fold and 1.22 ± 0.07-fold, respectively) compared to the parental A375 (Fig. 3e). While acidification of the medium with the A375-NTP-R cells was not as high as that of the A375-Hypoxia cells (1.37 ± 0.16-fold and 2.24 ± 0.19-fold, respectively), the NTP-resistant cells still showed significantly higher medium acidification ($p=0.0403$) compared to that of the parental A375 (Fig. 3f). Therefore, taken together, the NTP-resistant cell line also displayed more aerobic glycolysis as measured by the extracellular byproducts, lactate and medium acidification.

Not only did NTP-resistant cells appear to favor aerobic glycolysis, but they also demonstrated lower mitochondrial fitness compared to the parental. Using the Seahorse XF Cell Mito Stress assay, the stress test profiles revealed that the A375-NTP-R cells had a lower oxygen consumption rate (OCR) compared to the parental A375 (Fig. 3g). The resistant cell line demonstrated lower basal respiration ($p \leq 0.0001$) and non-mitochondrial respiration ($p \leq 0.0001$), and furthermore, resistant cells exhibited significantly decreased ATP production ($p \leq 0.0001$) and maximum rate of respiration levels ($p \leq 0.0001$) compared to the parental (Fig. 3h). These data further evidence a shift in cellular metabolism, as it appeared that the A375-NTP-R cells have decreased mitochondrial respiration compared to the parental A375 cells.

Another frequent and detrimental consequence of cells with increased glycolysis and higher extracellular acidification is an increase in the expression of immunosuppressive proteins on the surface of the cancer cells (Barsoum et al., 2014). Therefore, three immunosuppressive molecules, CD73, CD47, and programmed death-ligand 1 (PD-L1), were evaluated, using flow cytometry analysis (Fig. S5). While hypoxic cells showed increased CD73 and CD47 compared to the parental A375 (2.69 ± 0.56-fold and 1.19 ± 0.06-fold, respectively), these proteins appear

unchanged for the A375-NTP-R cell line (Fig. 3i, j). However, PD-L1 expression was significantly decreased in the NTP-resistant cells (0.75 ± 0.04-fold; p=0.0159) compared to that of parental A375 (Fig. 3k). In fact, this is in-line with our previous in vivo work in which we observed decreased PD-L1 expression on the tumor, following NTP treatment of B16F10 melanoma tumor-bearing mice (Lin et al., 2022). Therefore, based on the evaluation of three membrane molecules, the immunogenicity of the NTP-resistant cancer cells did not appear to decrease, as is common with cells having increased glycolysis and high extracellular acidification (Bartrons and Caro, 2007).

Taken altogether, the A375-NTP-R cells demonstrated higher glucose uptake, decreased mitochondrial respiration, and higher levels of lactate release and medium acidification compared to the parental A375 cells. These changes indicate a metabolic shift towards aerobic glycolysis, which has been shown to support drug resistance in cancer cells (Icard et al., 2018).

Differential response to NTP treatment between NTP-resistant and parental cells

Until now, we have reported the baseline alterations between the resistant A375-NTP-R cells and the parental A375 cells following the 12-week culture period. Here, we also evaluated and compared the immediate responses of both cell lines to NTP.

At the end of the 12-week culture period, both cell lines were seeded into 6-well plates, treated with NTP, and cultured for an additional 24 h, at 37 °C and 5% CO_2. The next day, untreated wells and NTP-treated wells were collected, and RNA was isolated and sequenced. RNAseq analysis was performed by comparing the NTP-treated to the untreated, for both the resistant and parental cell lines (Contrast: NTP vs Untreated). Following NTP treatment, both cell lines had 33 common DEGs (17 upregulated DEGs; 16 downregulated DEGs), while the A375-NTP-R cell line had more unique DEGs compared to the parental (Fig. 4a). Overrepresentation analysis (ORA) was performed on the upregulated DEGs using g:GOSt (g:Profiler, Estonia) for both cell lines, and genes were mapped to the gene ontology database (Raudvere et al., 2019). Interestingly, following NTP treatment, ORA revealed that the parental cell line resulted in more apoptotic overrepresented terms (10 out of 15; indicated in green), while the resistant cell line resulted in more terms associated with cell cycle arrest (9 out of 17; indicated in blue) and no apoptotic terms (Fig. 4b). The full list of DEGs (Table S1 and 2) and the functional terms from ORA (Table S3) are provided.

GSEA with the Hallmark gene set was also performed by contrasting the NTP-treated and untreated cells for resistant and parental cell lines (Fig. 4a). Only the P53 Pathway gene set was significantly enriched for both the resistant and parental cells, following NTP treatment, and only the NTP-treated parental A375 cell line demonstrated significant upregulation of the apoptosis pathway, ROS pathway, and EMT compared to untreated (Fig. 4a). On the other hand, GSEA of NTP-treated A375-NTP-R cells compared to the untreated, only revealed downregulation of the UV response and glycolysis pathways. GSEA between the NTP-treated resistant and parental cell lines (Contrast: $NTP_{Resistant}$ vs $NTP_{Parental}$) revealed that the Hedgehog Signaling pathway was upregulated, while TNFα Signaling via NFκB and Apoptosis pathways were significantly downregulated (Fig. 4c).

Taken together, it appeared that the NTP-resistant cell line and the parental A375 cell line respond differentially to NTP treatment. The data suggest that the parental A375 cells are more inclined to apoptotic pathways following treatment, while resistant A375-NTP-R cells are more inclined to cell cycle arrest. Therefore, it was worth further investigating the NTP-induced cell death mechanisms of resistant and parental A375 cells.

Differential cell death mechanisms following NTP treatment between NTP-resistant and parental cells

Based on the RNAseq analysis (Fig. 4), we further investigated the NTP mechanisms of action following treatment of NTP-resistant and parental cells, by performing a proliferation assay and an apoptosis assay. Cells were seeded into 24-well plates and treated with NTP on the following day in order to collect enough cells for subsequent analysis. Different NTP treatment energies were tested in resistant and parental cell lines to define comparable cell death treatment conditions for further molecular characterization (Fig. 5a). At a low treatment energy of 1.0 J, no significant difference in cell survival was measured between the two cell lines (p=0.1175), while at a higher energy of 3.8 J, the resistant cell line demonstrated higher survival compared to the parental (94 ± 2% vs 60 ± 3%, respectively; $p \leq 0.0001$). When NTP treatment energy was sufficiently high at 9.5 J, cell survival for both cell lines remained near 50% (47 ± 4% for the parental and 58 ± 3% for the resistant), and was once again, not statistically different (p=0.2350). Therefore, the 1.0 J (low NTP treatment; NTP_L) and the 9.4 J treatment (high NTP treatment; NTP_H) energies were used for all subsequent experiments to ensure that comparisons were made at equivalent levels of cell death, 24 h post NTP treatment.

To examine whether the NTP-resistant cells exhibited more cell cycle arrest following NTP treatment, as suggested from ORA (Fig. 4b), cells were collected 24 h after treatment and 10^4 live cells were re-seeded into 96-well plates. When cells reached a confluence of 20 ± 1%, live-cell imaging was performed to monitor their growth for 24 h. Cell proliferation was determined based on the confluence from phase-contrast images. Interestingly, only the resistant cells receiving NTP_H treatment showed an altered growth rate, as demonstrated by a higher confluence over time (Fig. 5b). Although no significant differences were measured between NTP-treated and untreated cells for both cell lines, at 18 h, NTP_H-treated resistant cells had grown significantly more compared to the NTP_H-treated parental cells (p=0.0395), which persisted up to 24 h (Fig. 5b). In fact, when normalized to their starting confluence, the NTP_H-treated A375-NTP-R cells showed a higher fold change compared to that of the parental NTP_H-treated A375 cells at the final, 24 h, timepoint (2.8 ± 0.1 vs 2.3 ± 0.1, respectively; p=0.183) (Fig. S6). Therefore, it appeared that the growth rate of NTP-treated resistant cells was not inhibited, as suggested by ORA, and in fact, A375-NTP-R cells receiving high energy NTP treatment demonstrated a higher proliferation rate.

To determine whether the A375 cells were more sensitive to apoptosis compared to the A375-NTP-R cells after exposure to NTP, cells were stained with Annexin V for phospholipid phosphatidylserine and measured with image cytometry, 24 h after NTP treatment. The Annexin V-positive cells were counted per confluent area and normalized to the corresponding untreated cells. High energy NTP treatment induced significantly higher Annexin V positivity for the parental cell line (2.60 ± 0.41-fold change; $p \leq 0.0001$), but not the resistant cell line (1.73 ± 0.23-fold change; p=0.0688) (Fig. 5c). Furthermore, the level of Annexin V positivity was significantly higher for the parental cells compared to the resistant cells at NTP_H-treatment (p=0.0172).

Caspase 3/7 was also measured as an indicator of apoptosis, and cells were stained and analyzed via image cytometry (Fig. 5d). When normalized to untreated cells, NTP treatment of the parental cells induced significantly higher caspase 3/7 positivity for both the low (2.64 ± 0.48-fold change; p=0.0164) and the high (4.42 ± 0.66-fold change; $p \leq 0.0001$) treatment energies, while NTP treatment of the resistant cells only induced caspase 3/7 positivity at the high NTP treatment energies (3.24 ± 0.37-fold change; p=0.0001). Moreover, NTP_H-treatment significantly induced higher caspase 3/7 levels for the A375 parental cells compared to the resistant A735-NTP-R (p=0.0230). Taken together, these data indicate that the A375-NTP-R cells were more resistant to apoptosis compared to the parental cells following NTP treatment, as suggested from the comprehensive RNAseq data (Fig. 4).

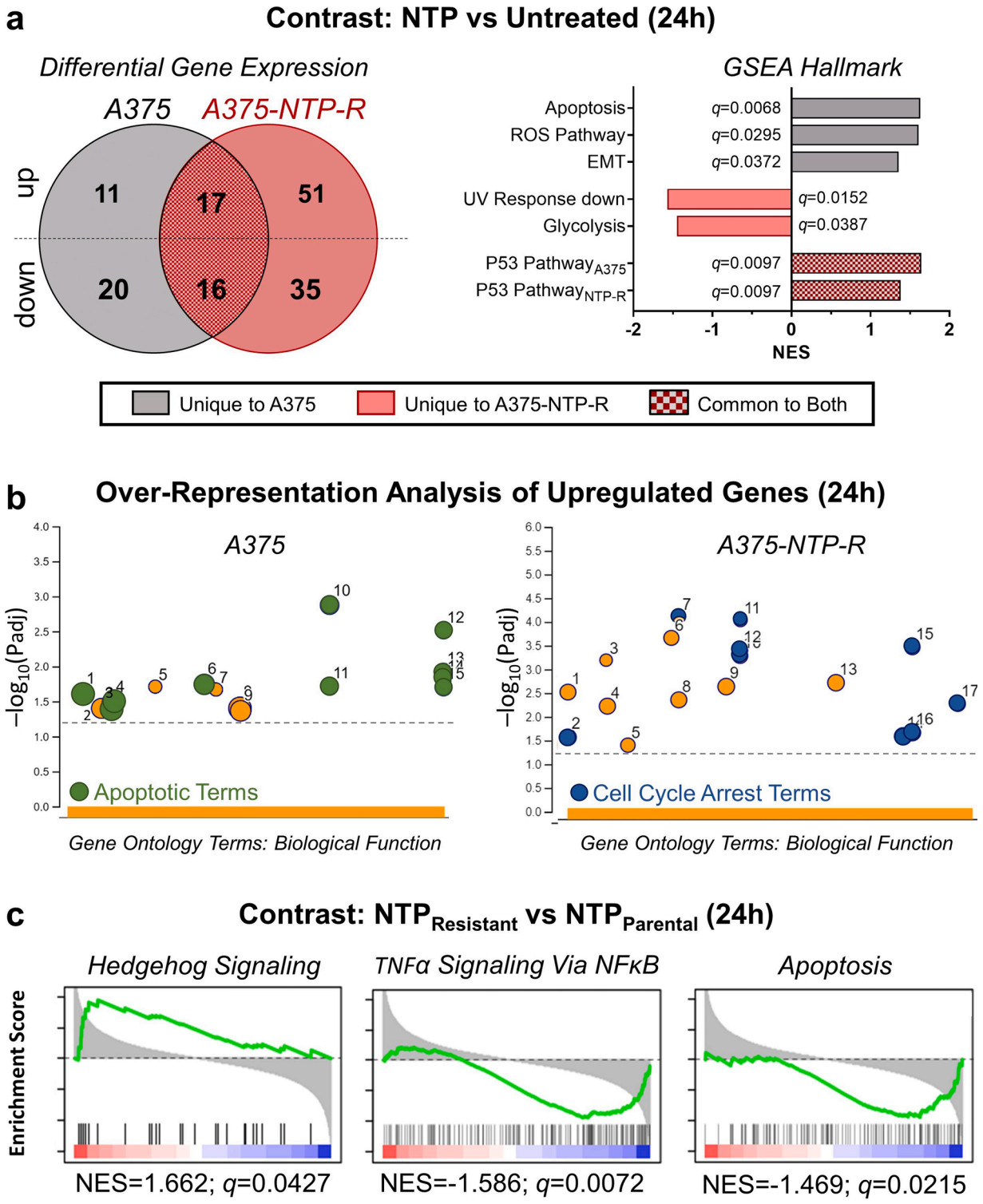

Fig. 4. NTP-resistant and parental cell lines demonstrated differential whole transcriptome responses to NTP. a EdgeR analysis revealed 33 common DEGs between the two cell lines, 31 unique DEGs for the parental A375 cells, and 86 unique DEGs for the A375-NTP-R cells. GSEA with the Hallmark gene set revealed one commonly enriched pathway (P53 Pathway) and two and three uniquely enriched pathways for both the A375-NTP-R and A375 cells, respectively. b Over-representation analysis of the upregulated DEGs, using g:GOSt, revealed more significant apoptotic terms for the parental A375 cells, and more significant cell cycle arrest terms for the resistant A375-NTP-R cells. The dashed line indicates the significant threshold. c GSEA was also performed by contrasting the NTP-treated A375-NTP-R cells ($NTP_{Resistant}$) and the NTP-treated parental A375 cells ($NTP_{Parental}$). The green line indicates the enrichment profile and the y-axis indicates the enrichment score based on the ranked list of genes. Here, it appears that the Hedgehog Signaling pathway was significantly more enriched in A375-NTP-R cells after treatment, while TNFα Signaling via NFκB and Apoptosis pathways were significantly downregulated compared to NTP-treated parental cells.

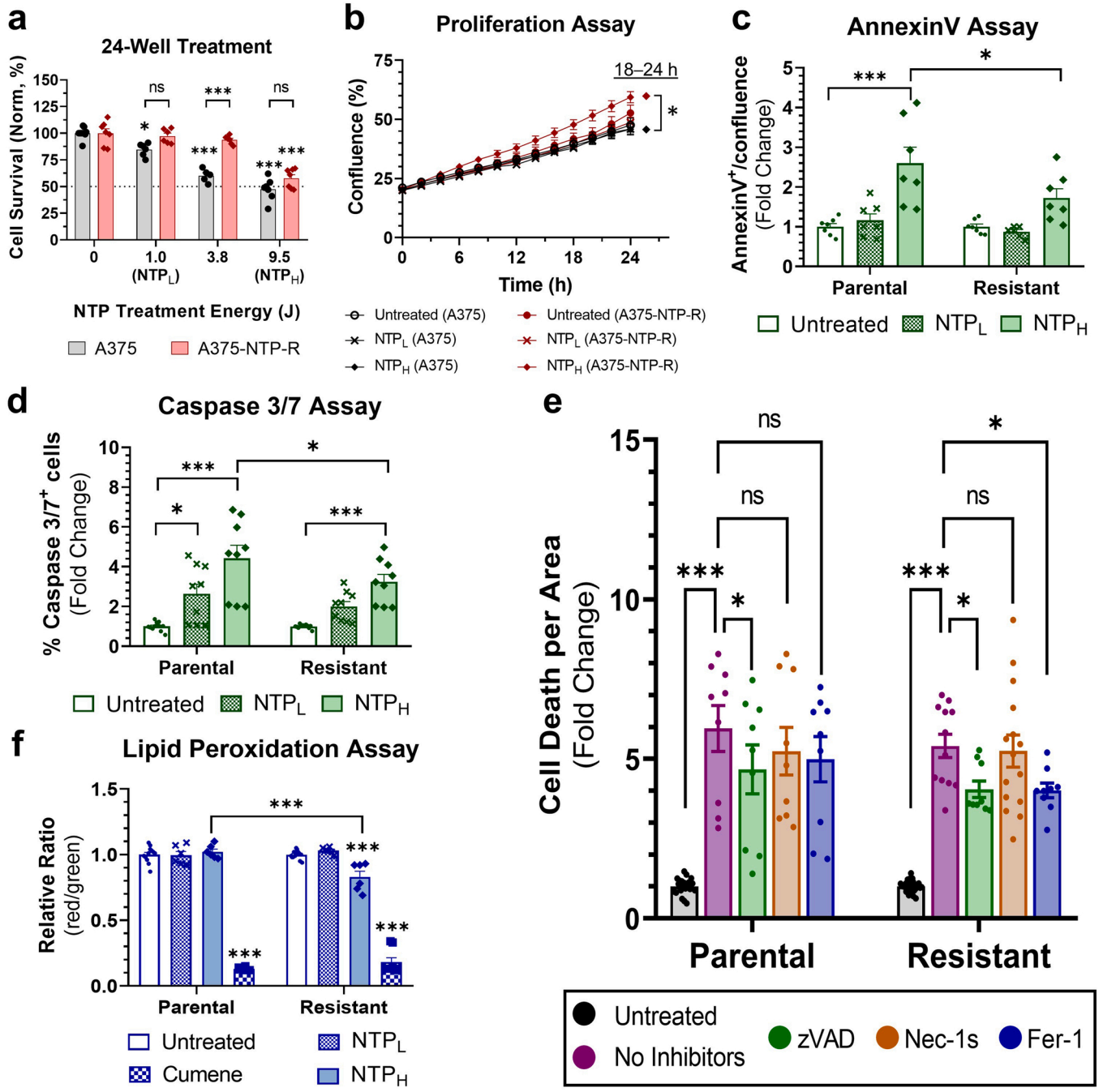

Fig. 5. Following exposure to NTP, the resistant A375-NTP-R cells demonstrated an altered response compared to the parental A375 cells. a Cells were seeded and treated in 24-well plates in order to collect enough cells for analysis, 24 h after NTP exposure. Different NTP treatment energies were used and the low (NTP_L) and high (NTP_H) treatments were used for subsequent experiments. b Cells were collected and seeded into 96-well plates, 24 h after exposure to NTP, and growth rate was assessed by measuring confluence with live-cell imaging for 24 h. Higher cell confluence was measured with the NTP_H-treated resistant cells compared to the NTP_H-treated A375, from 18 to 24 h. Statistical significance was calculated using the mixed-effect model with the Geisser-Greenhouse correction and the Tukey's multiple comparisons test. Apoptosis was evaluated with an c Annexin V assay and a d Caspase 3/7 assay, which confirmed that the parental cells were more sensitive to apoptosis at NTP_H treatment. e zVAD-fmk (zVAD), necrostatin-1 s (Nec1s), and ferrostatin-1 (Fer-1) were used to inhibit NTP-induced apoptosis, necroptosis, and ferroptosis, respectively. While zVAD reduced cell death for both the parental and resistant cells, Fer-1 only reduced cell death for the resistant cells. f A lipid peroxidation assay was therefore performed, which revealed that only NTP_H treatment of the resistant A375-NTP-R cells induced significant lipid peroxidation. Data here are represented as mean ± SEM and each biologically independent sample is shown. Statistical significance was calculated using the generalized linear mixed model, unless otherwise specified. * $p \leq 0.05$, * * $p \leq 0.01$, * ** $p \leq 0.001$ (more detailed p values are reported in the text).

To further examine the different NTP-induced cell death mechanisms between the parental and resistant cells, three inhibitors were used to analyze relative contribution of apoptosis (zVAD-fmk; zVAD), necroptosis (necrostatin-1 s; Nec1s), and ferroptosis (ferrostatin-1; Fer-1). Both parental and resistant cells were treated at NTP_H energies and a cell death stain was used to identify dead cells. Cells were analyzed at 24 h and the amount of cell death per confluent area was measured and normalized to the untreated. NTP_H-treatment induced equivalent cell death for both the parental (6.00 ± 0.72-fold change; $p \leq 0.0001$) and resistant (5.41 ± 0.37-fold change; $p \leq 0.0001$) cells compared to their

corresponding untreated cells, and the apoptosis inhibitor, zVAD, also significantly inhibited cell death for both the parental (4.67 ± 0.77-fold change; p=0.0384) and resistant cells (4.05 ± 0.26-fold change; p=0.0454), as expected (Fig. 5e). Nec-1 s did not significantly inhibit cell death for either cell line, and Fer-1 only significantly inhibited NTP treatment efficacy for the resistant cell line (4.01 ± 0.23-fold change; p=0.0365). Since, Fer-1 is a synthetic antioxidant that modulates lipid peroxidation, we examined whether A375-NTP-R cells were more prone to lipid peroxidation following exposure to NTP. A lipid peroxidation assay was performed 24 h following low and high energy NTP treatment of both parental and resistant cell lines. The cells were stained with the C11-BODIPY dye, a sensitive fluorescent reporter for lipid peroxidation which shifts from red to green fluorescence upon oxidation, and analyzed with flow cytometry. Whereas the ferroptosis inducer compound (Cumene) triggered a significant increase in lipid peroxidation, in the parental A375 cell line, indicated by a reduced ratio of red/green fluorescence ($p\leq0.0001$), the cells did not demonstrate any lipid peroxidation after NTP treatment (Fig. 5f). Conversely, NTP_H-treatment of the A375-NTP-R cells showed significant increase in lipid peroxidation (and significant reduction of the ratio of red/green fluorescence) compared to untreated ($p\leq0.0001$), which was also significantly lower than parental cells ($p\leq0.0001$). These data suggest that while NTP-resistant cells were less sensitive to apoptosis, they appear more prone to lipid peroxidation and ferroptosis.

Altogether, the resistant A375-NTP-R cells demonstrated a differential cellular response to NTP exposure compared to the parental A375. Following NTP treatment, the resistant cells demonstrated a higher growth rate (Fig. 5b) and lower Annexin V and Caspase 3/7 expression (Fig. 5c,d), which suggests reduced sensitivity for apoptosis. However, the resistant cells also appear to be more sensitive to lipid peroxidation and ferroptosis pathways following NTP (Fig. 5e).

Sensitive and resistant cell lines for 3D spheroid development

Following characterization of the NTP-resistant and parental cells in 2D monolayers, we attempted to evaluate NTP treatment response in a 3D spheroid model. 3D spheroids allow for better cell-to-cell interactions, extracellular matrix interactions, and cell heterogeneity,

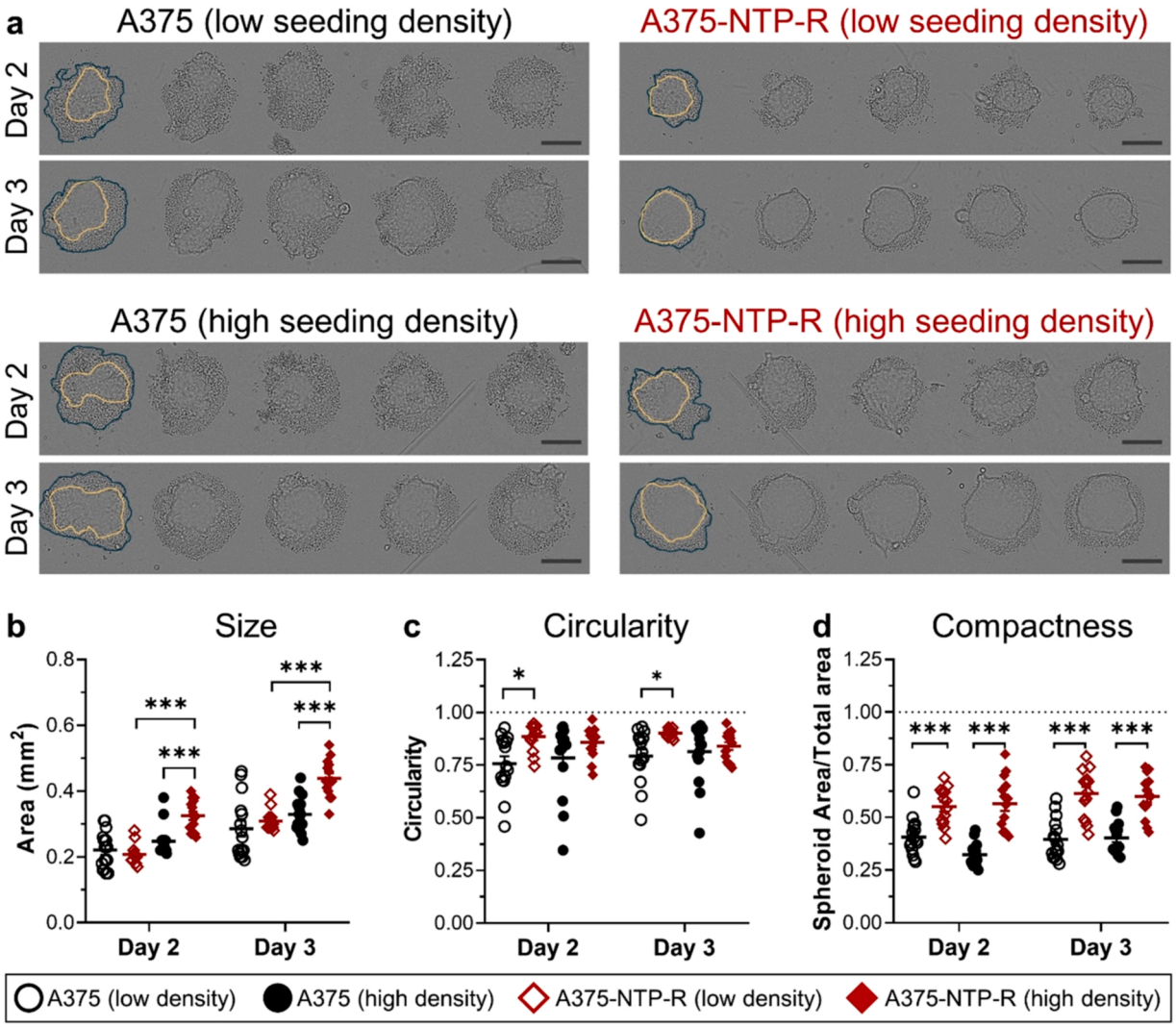

Fig. 6. Cellular physiology was altered in NTP-resistant melanoma cells for developing 3D cancer spheroids. a Representative microscope images (10x) of parental A375 and resistant A375-NTP-R spheroids from one independent experiment were taken with the Tecan Spark® Cyto on day 2 and 3 after cell seeding at low and high densities. The spheroid area (yellow outline) and the total area (blue outline) were manually annotated in ImageJ. b The spheroid area (yellow outline), was quantified in ImageJ and c the spheroid circularity was calculated. A dotted line at 1.00 indicates a perfect circle. d The total area was also quantified with ImageJ and spheroid compactness was calculated as a ratio of spheroid area over total area. A dotted line at 1.00 indicates a compact spheroid where cells do not fall out of the spheroid. Data here are represented as mean ± SEM and each biologically independent sample is shown. Statistical significance was calculated using the generalized linear mixed model. * $p \leq 0.05$, * * $p \leq 0.01$, * ** $p \leq 0.001$ (more detailed p values are reported in the text).

based on their spatial distribution: highly proliferating cells on the outer layer of the spheroid and quiescent or hypoxic cells on the inner layers (Shoval et al., 2017).

Both the NTP-resistant A375 cells and the sensitive parental cells were seeded into coated, round-bottom 96-well plates to make 3D spheroids, using 2 seeding densities (low: 3000 cells/well and high: 5000 cells/well). While the resistant A375-NTP-R cells were able to form circular and compact spheroids, the parental A375 cells were not (Fig. 6a). It was clear from the images, that the spheroid area (yellow outline) was much more circular in the A375-NTP-R group compared to the parental A375 group. Furthermore, the total area (blue outline), which includes cells that were not able to make compact spheroids, was much larger for the parental A375 group compared to the resistant. Spheroid area and circularity (calculated from the yellow outline) and spheroid compactness (ratio of spheroid area over total area) were quantified with manual image annotation in ImageJ (detailed in Materials and Methods).

At low seeding densities, both NTP-resistant and parental cells produced spheroids with similar areas on both day 2 (0.21 ± 0.01 mm^2 and 0.22 ± 0.02 mm^2, respectively; p=0.8807) and day 3 (0.31 ± 0.01 mm^2 and 0.29 ± 0.02 mm^2, respectively; p=0.6879), but the NTP-resistant spheroids were significantly more circular (day 2: 0.89 ± 0.04 versus 0.76 ± 0.02, respectively; p=0.0215 and day 3: 0.90 ± 0.01 versus 0.79 ± 0.03, respectively; p=0.0308) (Fig. 6b, c). While increasing seeding density only increased the NTP-resistant spheroid area on both days ($p \leq 0.001$), it did not significantly improve spheroid circularity (Fig. 6c). Furthermore, spheroid compactness remained significantly lower for the parental A375 spheroids compared to the A375-NTP-R spheroids ($p \leq 0.001$), irrespective of seeding density (Fig. 6c).

Taken together, it is clear that prolonged exposure to NTP also had significant consequences on cell physiology that impacted the development of 3D cancer spheroids. Since the starting spheroid area, circularity, and compactness between the NTP-resistant and parental cells were significantly different, they could not be used to compare NTP treatment effects. Alternative 3D models will be required for further evaluation of NTP resistance.

Discussion

Acquired resistance to cancer therapy remains a great challenge in

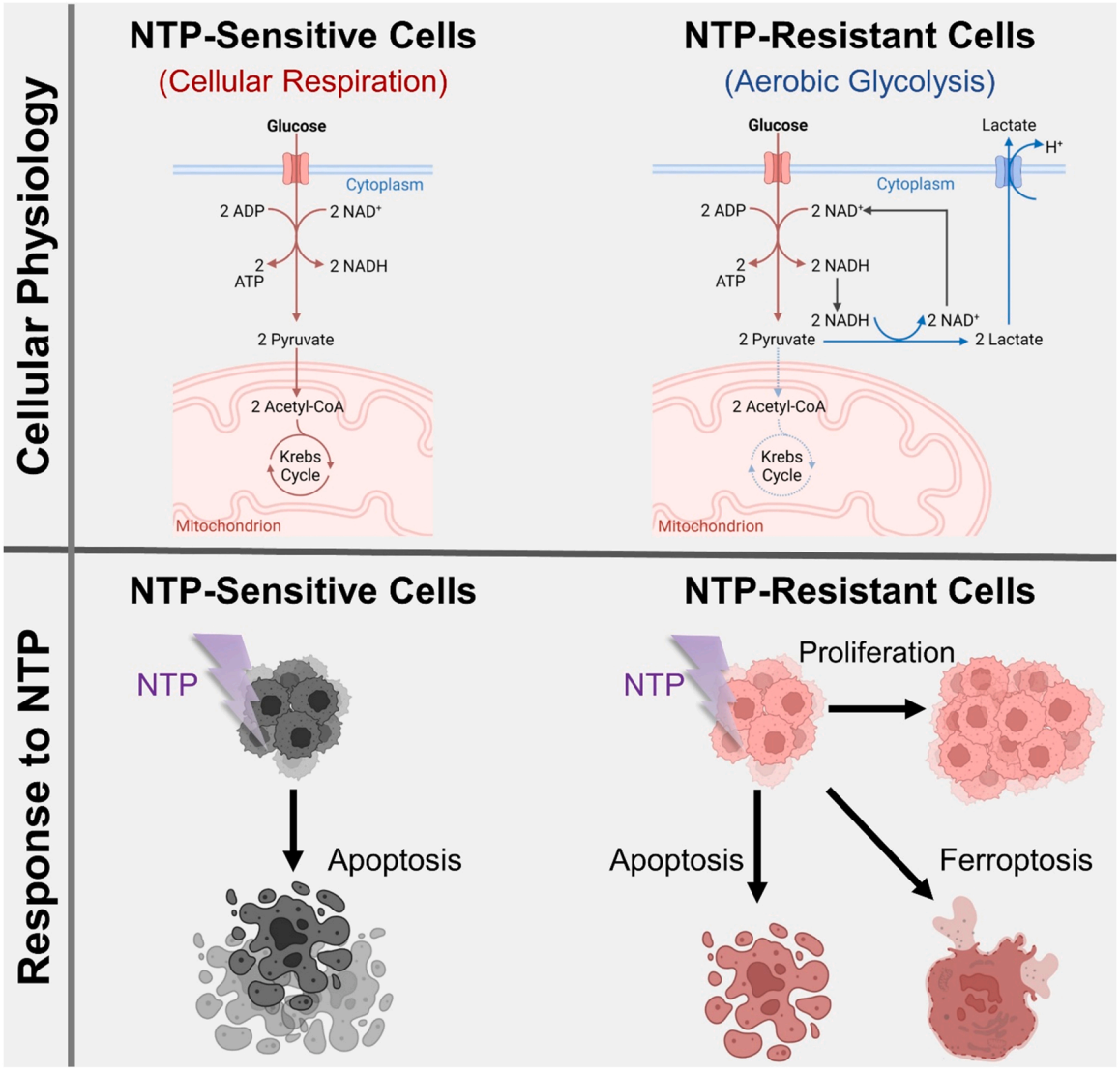

Fig. 7. New insights and hypothesis for NTP sensitivity versus resistance. Based on our results, NTP-resistant cells had altered cellular physiology and response to NTP. We propose that metabolic rewiring, particularly a preference towards aerobic glycolysis, is partially responsible for resistance towards NTP. Furthermore, while NTP-sensitive cells were more prone to apoptosis, NTP-resistant cells demonstrated more lipid peroxidation, which suggests that they are more vulnerable towards ferroptosis. Additionally, we observed higher proliferation rates in NTP-resistant cells, which may contribute to their higher overall survival after treatment.

clinical oncology and, therefore, should be evaluated for novel and emerging cancer treatment strategies, such as NTP. We developed, for the first time, an NTP-resistant cell line and performed a detailed evaluation of its physiological alterations and responses to NTP. NTP-resistant cells exhibited a metabolic shift towards aerobic glycolysis from cellular respiration, compared to the parental cells (Figs. 2 and 3). Furthermore, NTP-resistant cells demonstrated reduced sensitivity to apoptosis, higher proliferation rates, and increased susceptibility to lipid peroxidation-driven ferroptosis in response to NTP exposure, compared to their parental counterparts (Fig. 5). These data highlight important insights and a new hypothesis into the pathways and mechanisms of action for NTP sensitivity versus resistance (Fig. 7). In a broader sense, our method for developing cells with acquired NTP resistance provides a valuable tool for further in-depth investigations into NTP treatment mechanisms and applications for other cancer types.

While several studies in the past have attempted to investigate cell sensitivity to NTP, several confounding factors have often been overlooked, which led to misleading results (Georgescu and Lupu, 2010; Zucker et al., 2012; Guerrero-Preston et al., 2014). In many of these studies, cancer cell lines were compared to their non-malignant counterparts. However, due to limitations in commercially available cell lines, often different cell types (e.g. epithelial vs fibroblasts) were used. Furthermore, not all cell lines use the same cell culture medium. Since the NTP-generated ROS are known to be the main biological effectors, the scavenging capacity of different cell culture media cannot be overlooked (Tanaka et al., 2021). In our previous report, we demonstrated how cell type, cancer type, and cell culture medium can, in fact, affect NTP treatment outcome and selectivity (Biscop et al., 2019). As such, our method for generating NTP-resistant cells from a previously sensitive cell line is highly advantageous and overcomes many of the limitations associated with studying NTP sensitivity. Not only do the cell lines have the same starting genetic background, they also require the same cell culturing methods, and by culturing the parental cells in parallel with the NTP-exposed cells, the effect of cell passage can be accounted for. Indeed, this method helped reduce excess variability in comparing NTP sensitive and resistant cells, especially in RNAseq analysis. Therefore, our method could be applied to other cell lines and cancer types and provide a valuable means to study NTP sensitivity.

It has long been hypothesized that cells with faster proliferation rates and higher basal intracellular ROS levels are more sensitive to NTP treatment. While we did not observe any changes to the basal proliferation rate for the NTP-resistant cells compared to the parental (Fig. 1b), we did observe lower baseline levels of intracellular ROS (Fig. 1c). In recent work, more detailed hypotheses explaining the cancer cells' sensitivity to NTP treatment have emerged, including: higher aquaporins expression in the plasma membrane, facilitating ROS transport into cells (Yan et al., 2015), higher cellular ability for redox balance (Tanaka et al., 2017), and lower cholesterol content in the plasma membrane, which allows for easier ROS transport into cells and easier pore formation (Van der Paal et al., 2017, 2016). Bekeschus et al. (2021) performed a thorough investigation to test these hypotheses, screening for several factors in 38 human cell lines in order to correlate them to NTP sensitivity. Interestingly, from their screening, neither aquaporins nor redox-related surface enzymes, two factors that would contribute to higher oxidative damage from NTP treatment, were found to have a clear correlation. On the other hand, the cholesterol content in cell membranes had a significant correlation with NTP resistance (Spearman $r = 0.68$), though it was not the highest. Using resazurin, a cell-permeable dye that is reduced in the mitochondria, as an indicator of metabolic activity, they found that this parameter had the highest correlation with NTP sensitivity (Spearman $r = 0.76$). Thus, they also suggested that cell metabolism may serve as a novel hypothesis for NTP sensitivity (Bekeschus et al., 2021). Our data here on isogenic sensitive and resistant cell lines compliment their results. From RNAseq analysis, NTP-resistant cells showed altered metabolism both in the top gene clusters (Fig. 2b) and GSEA (Fig. 2c). Furthermore, our functional evaluations of cellular metabolism also indicate metabolic rewiring, and suggest that NTP-resistant cells have more hypoxic signatures and favor aerobic glycolysis compared to cellular respiration (Fig. 3).

Hypoxic signatures and metabolic rewiring have been highly associated with chemotherapy (Belisario et al., 2020), radiation therapy (Wang et al., 2019), and even immunotherapy resistance (Kopecka et al., 2021). This is due to enhanced pro-survival pathways, reduced apoptosis, increased DNA repair, and even changes in drug targets. Of particular importance, upregulation of HIF-1α, which we measured in NTP-resistant cells (Fig. 3a), is highly tied to several drug resistance pathways. HIF-1α regulates multiple genes and pathways, including adenosine triphosphate-binding cassette (ABC) transporters, which can efflux several chemotherapeutic drugs (Comerford et al., 2002). This type of resistance mechanisms is unrelated to the drug structure or mechanism of action, thereby contributing to multidrug resistance in cancer (Belisario et al., 2020). Suppression of mitochondrial activity has also been suggested to drive HIF-associated treatment failure for both chemotherapies and radiation therapies with mechanisms involving direct DNA damage or ROS-induced cellular damage (Belisario et al., 2020; Wang et al., 2019). HIF-1α participates in protecting against DNA damage, including through activation of repair enzymes such as DNA-dependent protein kinase (Um et al., 2004; Wrann et al., 2013; Rohwer and Cramer, 2011). Interestingly, mitochondrial dysfunction and HIF-1α upregulation can lead to an increase in ROS accumulation, which triggers higher adaptive responses to mitigate oxidative damage (Belisario et al., 2020; Rohwer and Cramer, 2011). This protective response, in turn, can neutralize ROS-induced chemo- and radio-therapeutic drugs, thus contributing to resistance. Indeed, we observed that NTP-resistant cells exhibited decreased intracellular ROS (Fig. 1c), and since the NTP mechanism of action is via ROS generation and delivery, this is a mechanism that should be further investigated. Finally, tumor-derived lactate and environmental acidity from metabolic rewiring has also been reported to impair anti-cancer immunity by increasing immunosuppressive proteins and suppressing cytotoxic T cell and NK cell function (Elia et al., 2022; Brand et al., 2016; Ding et al., 2021). This in turn can affect cancer immunotherapies, and several studies have already demonstrated that the toxic tumor microenvironment (TME) inhibits the efficacy of immune checkpoint blockade therapies (Kopecka et al., 2021; Ding et al., 2021; Scharping et al., 2017). Interestingly, while measuring higher lactate and medium acidification in the NTP-resistant cells (Fig. 3e,f), we did not observe increased expression of immunosuppressive CD47 and CD73, and even measured a significant decrease in PD-L1 (Fig. 3i, j, k). These results are in-line with our previous work and highlight the protein-specific response to NTP treatment. In the past, our lab has reported that NTP was able to immediately oxidize immunosuppressive proteins, including CD47, via oxidation of salt-bridges responsible for conformational changes (Lin et al., 2021a). These effects were rapid, and based on our results here (Fig. 3i, j), it appeared that recurrent NTP treatment did not sustain decreased CD47 (or CD73) expression in the A375-NTP-R cells, at baseline. On the other hand, recurrent NTP treatment induced a sustained decrease in PD-L1 expression (Fig. 3k), which we have also observed and reported in our previous in vivo work (Lin et al., 2022). Therefore, prolonged exposure of cells to NTP could affect the expression of various cancer proteins. Since more evidence of the immunotherapeutic properties of NTP are starting to accumulate (Khalili et al., 2019), deeper understanding into how NTP-resistance affects immunological aspects of the TME is required, especially in the context of combination with immune checkpoint inhibitors.

Besides significant basal alterations in cell physiology of NTP-resistant cells versus the sensitive parental cells, the two cell groups also had differential responses to NTP (Figs. 4 and 5). While NTP-resistant cells demonstrated reduced apoptosis sensitivity (Fig. 5c,d), they appeared to be more susceptible to lipid peroxidation and ferroptosis (Fig. 5e,f). Ferroptosis is a distinct programmed cell death process with unique pathways (e.g. glutathione peroxidase (GPX4) inactivation,

lipid peroxide accumulation) and morphological features (e.g. shrunken mitochondria, disrupted membrane) (Xu et al., 2019). The investigation into the ability of NTP to induce ferroptosis has only just started, and in our recent work, we have reported on the capacity of NTP-generated ROS to induce ferroptosis in glioblastoma cell lines (Van Loenhout et al., 2021). In our current study, statistically significant changes in lipid peroxidation and ferroptosis following NTP treatment was only detected in the NTP-resistant cells (Fig. 5f). Ferroptosis induction has been used as a potential strategy for overcoming resistance in apoptosis-inducing chemotherapies or for eliminating drug-tolerant predictor cells, which have survived several rounds of therapy (Xu et al., 2019; Li et al., 2020; Viswanathan et al., 2017). In fact, several studies have reported that therapy-resistant cancer cells were more dependent on the GPX4 pathways and more vulnerable to ferroptotic cell death (Viswanathan et al., 2017; Hangauer et al., 2017; Hassannia et al., 2019), and reports of the immunogenic potential of ferroptosis are also emerging (Van Loenhout et al., 2021; Efimova et al., 2020). The stemness features of NTP-resistant cells are also of significant interest, as ferroptosis sensitivity and aerobic glycolysis have been linked to epithelial-mesenchymal transition (EMT) and cancer cell stemness (Yadav et al., 2020; De Backer et al., 2022; Lee et al., 2020; Friedmann Angeli et al., 2019). Indeed, several of the upregulated DEGs we measured in the NTP-resistant cells (e.g. *HDAC11*, *SOX11*, *MYC*; Fig. 2a) have also been linked to this phenomenon. Taken together, our results align with the current literature on ferroptosis, and suggest that NTP could be an interesting strategy to be combined with existing cancer therapies to overcome drug-resistance. However, more investigation into the mechanisms of NTP action, particularly on its ferroptotic potential and EMT, is greatly needed. It is important to highlight here, that in addition to NTP sensitivity, our A375-NTP-R cell line and the parental A375 can also provide an advantageous model to study ferroptosis pathways, due to their genetic similarity and differential lipid peroxidation response.

Following characterization of the NTP-resistant and sensitive cells in 2D monolayers, the next step includes evaluating the resistant and parental cells in 3D cancer models that better represent the solid tumor structure and TME. Here, we have attempted to make 3D spheroids using both the resistant and sensitive A375 cells, but the area, circularity, and compactness were significantly different (Fig. 6). This makes the spheroid model unsuitable for further evaluation of NTP treatment resistance. A375 melanoma cells are known to be difficult for making spheroids, partially due to the morphology of the disease (Shoval et al., 2017; Han et al., 2021). Interestingly, the A375-NTP-R cells were able to form more circular and compact spheroids (Fig. 6). It has previously been reported that cells with higher levels of E-cadherin formed more compact spheroids, and are usually more resistant to various therapies (Han et al., 2021). Although differences in E-cadherin and N-cadherin levels were not detected from the RNAseq analysis, this should be confirmed with more downstream molecular analysis. While the cancer spheroid model may not be suitable for the melanoma cells (or require more complex culturing methods (Shoval et al., 2017)), this could be of interest for further investigation of NTP-resistance with other 3D cancer models. Additional models that include components of the TME, such as the chick chorioallantoic membrane in ovo model or in vivo mouse models (e.g. xenograft, humanized) (Avram et al., 2017), should also be considered in future studies, as the TME is reported to contribute to therapy resistance (Baghban et al., 2020). There is also increasing evidence that NTP can affect multiple aspects of the TME, though these studies have predominately focused on the anti-cancer and immunologic effects (Clemen et al., 2020; Yusupov et al., 2021; Privat-Maldonado et al., 2022; Van Loenhout et al., 2019; Freund et al., 2020). In addition to CD47, our lab has also demonstrated that NTP is able to oxidize hyaluronan, an essential component of the extracellular matrix, and modulates cancer cell proliferation (Yusupov et al., 2021). Furthermore, NTP treatment of cancer-associated fibroblasts, pro-tumorigenic and immunosuppressive components of the TME, was reported to increase anti-cancer immune responses and did not change the metastatic potential of the tumor (Privat-Maldonado et al., 2022; Van Loenhout et al., 2019). In the future, more studies should focus on the influence of the TME on NTP therapy resistance, and the use of NTP-resistant cell lines in these complex 3D models could be of great value.

In our study, NTP-resistant cells were developed and evaluated in one melanoma cell line, which we acknowledge as a limitation of the study for generating broader conclusions. However, as this is the first time NTP-resistant cells have been developed, our methods can serve as a blueprint for future studies and should be applied to more cell lines and cancer types. Although we have gained valuable insights into potential metabolic rewiring of cell death pathways following acquired NTP-resistance, a more detailed understanding of cell- and/or cancer-specific responses to NTP will require additional cancer treatment applications. In addition, more in-depth evaluation and validation of activated pathways should be performed. This includes detailed analysis of aerobic glycolysis-associated proteins as well as ferroptosis- and necroptosis-associated proteins. Furthermore, it would be of great interest to investigate other modalities of cell death, such as pyroptosis, and assess the immunogenicity of NTP-resistant cells. Lastly, it is of added value to further investigate NTP resistance in advanced 3D cancer models that mimic the complex TME. These insights will not only bring about deeper fundamental understanding into NTP sensitivity and acquired resistance, but also inform on strategic combination strategies with existing cancer therapies and provide the first steps towards identifying potential treatment biomarkers for NTP therapy.

Materials and methods

Cell culture and NTP treatment

The parental malignant human melanoma cell line (A375) was obtained from ATCC (CRL-1619TM) and cultured in Dulbecco's modified Eagle's medium (DMEM), which contained 4×10^{-3} M L-glutamine and supplemented with 10% fetal bovine serum, 100 U mL^{-1} penicillin, and 100 μL of streptomycin. The cells were incubated at 37 °C in a humidified atmosphere with 5% CO_2 and plated in 24-well plates (1.5×10^5 cells/well) 1 day before the weekly NTP treatment. NTP was generated using a microsecond-pulsed DBD plasma system as described in our previous studies (Lin et al., 2022, 2021a, 2021b). Briefly, the power supply (Megaimpulse Ltd., Russia) generated a 30 kV pulse with a rise-time of 1–1.5 μs and a pulse width of 2 μs. The energy per pulse of the discharge was measured to be 1.8 mJ/pulse, and the NTP treatment energy was calculated by multiplying energy per pulse with pulse frequency and treatment time (Bonzanini et al., 2021). The medium was removed from the well right before treatment and the DBD electrode was lowered into the well and fixed at 1 mm distance from the cells using a z-positioner. NTP was then discharged directly on the cells for 10 s at the defined frequency, starting at 100 Hz. Following treatment, 500 μL of fresh medium was immediately replenished in the well. The NTP treatment energy was increased every 2 weeks by increasing the pulse frequency by 100 Hz over a period of at least 12 weeks and up to 1000 Hz, while the parental A375 cell line was cultured and passaged in parallel. The resistant cells were maintained by treating them weekly at 700 Hz for 10 s. Mycoplasma testing was performed to ensure that cells remained uncontaminated and STR analysis authenticated the cell lines with the A375 profile.

3D spheroid culture method

For spheroid cultures, the A375 cells were seeded into specialized round-bottomed, hydrogel coated 96-well plates (ultra-low attachment plates, ULA, Corning® 7007, Corning). Cell suspensions were prepared at low (3×10^4 cells/well) and high (5×10^4 cells/well) concentrations in complete media, supplemented with 2% Matrigel (8.6 mg/mL, Corning) to enhance spheroid formation. Cells were centrifuged for

10 min at 1000 RPM and incubated at 37 °C and 5% CO_2. Spheroids were imaged at 10x with the Spark® Cyto (Tecan, Switzerland), 2 and 3 days after seeding, and images were analyzed with ImageJ (Java 1.8.0_112). The outline of the spheroid was manually traced as well as the total cell area, which includes cells that were not a part of the spheroid. The area of both the spheroid and total cell area was measured with the ImageJ plugin, and circularity was calculated: $circularity = 4\pi \times \frac{Area}{Perimeter^2}$. The compactness of the spheroids was also calculated: $compactness = \frac{Spheroid\ Area}{Total\ Cell\ Area}$.

Colony forming assay

The colony forming assay was performed according to standard protocols (Franken et al., 2006). Optimization experiments for plating efficiency was first performed and it was determined that seeding of 100 cells in 6-well plates had a high plating efficiency of 85%. Following NTP treatment (0—18 J), cells were detached and serial-diluted to seed 100 cells per 6-well plate, along with untreated controls. After 7 days of culture at 37 °C and 5% CO_2, cells were fixed with glutaraldehyde (6.0% v/v) and stained with crystal violet (0.5% w/v). Crystal violet was then washed away with PBS and two independent researchers counted the colonies. The mean of the counts was used to calculate the surviving faction (SF): $SF = \frac{no.of\ colonies\ formed\ after\ treatment}{no.of\ cells\ seeded \times plating\ efficiency}$.

Cell survival assay with image cytometry

Following NTP treatment, cells were incubated for 24 h at 37 °C and 5% CO_2, and then dual-stained with a nuclear dye, Hoechst (2 μM; 62249, ThermoFisher Scientific) in 0.3% Tween and a cell death stain, Incucyte® Cytotox Green (0.05 μM; 4633, Sartorius), using the D300e Digital Dispenser (Tecan, Switzerland). Cells were incubated with the dyes in the well for 45 min before brightfield and fluorescence whole-well imaging (2x) with the Spark® Cyto (Tecan, Switzerland). Total cells (Hoechst) and dead cells (Incucyte® Cytotox Green) were counted and analyzed with the Spark Control™ Image Analyzer, and cell survival was calculated for each well: $Cell\ survival(\%) = \frac{Total\ Cells - Dead\ Cells}{mean(Total\ Untreated\ Cells)}$.

Cell survival over the log transform of NTP treatment energy was calculated and nonlinear regression (log(inhibitor) vs. normalized response-variable slope) was performed using GraphPad Prism 9 (Dotmatics, UK).

Proliferation assay

To measure baseline proliferation of NTP-resistant and parental cells, cells were detached from cell culture flasks, counted, and seeded into 96-well plates (1.0×10^4 cells/well). In order to measure proliferation of NTP-resistant and parental cells following NTP treatment, cells were detached from 24-well plates, 24 h after exposure to NTP, and the same number of live cells was seeded into 96-well plates for all treatment conditions (1.0×10^4 cells/well). Following cell seeding, plates were incubated in the Incucyte® ZOOM live-cell imager (Sartorius, Germany) at 37 °C and 5% CO_2, and phase-contrast images were taken every 2 h. Confluence was measured with the Incucyte software v2018A and graphed as a measure of cell growth and proliferation.

Intracellular ROS assay

Cells were detached from cell culture flasks, counted, and seeded into 96-well plates (1.0×10^4 cells/well) and incubated at 37 °C and 5% CO_2 for 24 h. CellROX® Green Reagent (C10444, InvitrogenTM) was then added to each well (2.5 μM/well) and imaged every 2 h in the Incucyte® ZOOM live-cell imager (Sartorius, Germany). Total green intensity was measured with the Incucyte software v2018A and graphed to indicate intracellular ROS levels.

RNA sequencing analysis

For RNA sequencing, both NTP-resistant and parental cells were seeded into 6-well plates (1.5×10^5 cells/well) and incubated overnight. On the next day, cells were NTP-treated at 9.5 J and collected 24 h later for RNA extraction along with the untreated controls. Total RNA was extracted and purified using the PureLink RNA Mini Kit (Invitrogen), according to the manufacturer's protocol. An Epoch spectrophotometer (BioTek, USA) was used to quantify RNA concentration and purity by measuring absorbance at the 260/280 nm ratio. Samples were frozen in dry ice and sequenced at the Genomics Core Leuven (Leuven, Belgium). Reads were aligned to the human GRCm38 (Ensembl, "top-level" assembly) reference genome with STAR v2.7.2b using default alignment parameters (Dobin et al., 2013), and it was also used to generate gene counts tables (−-quantMode GeneCounts).

RNAseq analysis was performed on the BigOmics Platform (BigOmics, Switzerland). Differential gene expression was performed with EdgeR and GSEA was performed using the KEGG and Hallmark gene sets, 2 well-established gene sets, from the Molecular Signatures Database (Broad Institute, USA) (Subramanian et al., 2005). False discovery rate was set to $q = 0.05$.

Western blotting

To evaluate the induction of a hypoxic response in cancer cells (parental, NTP-resistant and hypoxic A375 cells), expression of HIF-1α and its downstream gene BNIP3 was evaluated using Western blotting. In short, cells were put on ice, washed with ice-cold PBS and lysed using a non-reducing lysis buffer complemented with complete Protease Inhibitor Cocktail (Roche). The lysate was heated at 100 °C for 5 min prior to freezing down. Protein content of the cell lysates was normalized following determination using the Pierce BCA Protein Assay Kit (23227, Thermo Scientific), according to the manufacturer's instructions, and 10% bromophenol blue and 10% dithitreitol (R0861, Thermo Scientific) were added. Samples were loaded onto a 4–20% Mini-PROTEAN TGX Precast Protein gel (4561096, Bio-Rad Laboratories) for electrophoresis at 100 V during 1.5 h. Next, the proteins were transferred onto an Immobilon-P PVDF membrane (IPVH00010, Merck Millipore) at 100 V during 1 h. Blocking was done for 1 h in 5% milk powder (70166, Sigma-Aldrich) prior to overnight staining with primary antibodies at 4 °C: mouse monoclonal anti-HIF-1α (1:1000, 610959, BD Pharmingen), rabbit polyclonal anti-BNIP3 (1:1000, HPA003015, Atlas Antibodies) and mouse monoclonal anti-β-actin (1:5000 – only for 10 min, A1978, Sigma-Aldrich). The following day, staining with respective anti-mouse and anti-rabbit HRP-labelled secondary antibodies (1:2000, 7076 S and 7074 S, Cell Signaling) was performed for 1 h. The chemiluminescent signal was developed using the Luminata Forte Western HRP Substrate (Merck Millipore) and detected using an Amersham Imager 680 (GE Healthcare). ImageJ software was used to quantify the relative density of the Western Blot bands for normalizing HIF-1α and BNIP3 expression to actin. Data are then normalized to the mean of the parental A375 and represented as fold change.

Glucose uptake analysis

Both cell lines were cultured in 24-well plates with glucose-free media and 24 h after cell seeding, 2-(N-(7-Nitrobenz-2-oxa-1,3-diazol-4-yl)Amino)− 2-Deoxyglucose (2-NBDG) was added at a concentration of 30 μM. 2-NBDG is a fluorescent glucose analog, which will be taken up by cells in the absence of glucose. Following 30 min of incubation with 2-NBDG, cells were collected and analyzed using flow cytometry analysis using the CytoFLEX flow cytometer (Beckman Coulter, USA). Flow cytometry analysis was performed on FlowJo v10.7.1 (FlowJo LLC, USA).

Lactic acid and pH analysis

Cells were cultured for 24 h, and then the media were collected for analysis of lactic acid and pH. Lactic acid was measured using a StatStrip Xpress Lactate Meter (Nova Biomedical, USA) and pH was also measured using a pHenomenal® pH1100H, pH meter (VWR, USA), following calibration and manufacturing instructions. Cell-free culture medium at normoxic and hypoxic conditions was also measured for lactate and pH, and the value was subtracted from all experimental measurements to measure changes introduced by the cells (Δlactate, ΔpH). Cells were also detached and counted, and both Δlactate and ΔpH was quantified per 10^6 cells. Data were then normalized to the mean of the parental and represented as fold change.

Seahorse assay

Mitochondrial respiratory function was examined using Seahorse XFp Cell Mito Stress Test Kit (Cat. #103010–100, Agilent Technologies, Santa Clara, CA, USA) according to the manufacturer's instructions. Briefly, 1.5×10^4 cells/well resuspended in 80 μL complete DMEM were seeded in an XFp miniplate (3 wells with A375-NTP-R cells and 3 wells with parental A375 cell). Twelve hours later, XF DMEM (assay medium), supplemented with Seahorse XF Glucose (10 mM), Seahorse XF Pyruvate (1 mM) and Seahorse XF L-Glutamine (2 mM) was used to rinse the cells (60 μL of growth medium is removed, 200 μL of assay medium is added, 200 μL medium is removed and 160 μL of assay medium is added) and the cell culture miniplate was introduced into a 37 °C non-CO_2 incubator for 45 min to 1 h prior to the assay. The cell culture XFp miniplate was loaded into the Seahorse XFp analyzer (Seahorse Biosciences, Agilent Technologies, Santa Clara, CA, USA) and real-time oxygen consumption rate was measured for 1.5 h. First baseline respiration was measured (Basal OCR) prior to mitochondrial perturbation by sequential injection of 1.5 μM oligomycin (a complex V inhibitor to decrease the electron flow through ETC); 1 μM FCCP (the uncoupling agent to promote maximum electron flow through ETC); and a mixture of 0.5 μM rotenone and 0.5 μM antimycin (complex I and complex II inhibitors, respectively, to shut down the mitochondria-related respiration).

Immunological evaluation with flow cytometry

To evaluate the expression of immunosuppressive proteins on the surface of the cancer cells (parental, NTP-resistant and hypoxic A375 cells), immunosuppressive markers CD73, CD47, and PD-L1 were evaluated using a multicolor flow cytometric panel. In short, cells were harvested, washed with ice-cold flow cytometry staining (FACS) buffer, and adjusted to 2×10^5 for all cellular counterparts and controls. Prior to antibody staining, cell suspensions were blocked for 30 min at 4 °C with human serum (Normal, Sigma-Aldrich BVBA, 26020100) to avoid aspecific binding of antibodies. The multicolor antibody panel consisted of CD73/APC (130–111–909, Clone REA804, Miltenyi Biotec), CD47/PE (556046, Clone B6H12, BD Pharmingen) and PD-L1/BV786 (563739, Clone MIH1, BD Biosciences), combined with Live-Dead Aqua (L34957, ThermoFisher Scientific) for viability staining. Fluorescence Minus One (FMO) controls were prepared in parallel with the full antibody cocktail. Cell suspensions were stained in the dark for 30 min at 4 °C, washed with FACS buffer, centrifuged for 5 min at 1500 rpm at 4 °C, and resuspended again in FACS buffer before measurement. Acquisition was done using the NovoCyte Quanteon flow cytometer (Agilent) and subsequently analyzed using the FlowJo software v10.7.1 (FlowJo LLC, USA). The mean fluorescence intensity (MFI) of the samples was subtracted from the FMO controls to provide corrected values (ΔMFI). Fold change was calculated based on normalization to the mean ΔMFI of the untreated.

Cell death inhibitors

To determine which cell death pathways are activated, inhibitors were used to block specific cell death pathways. The parental and resistant A375 cells were seeded in triplicate in a 24-well plate and incubated for 24 h at 37 °C. After incubation, the cell culture medium was removed and replaced with fresh medium containing 1 μM of SYTOX Green Nucleic Acid Reagent (S7020, Invitrogen). Next, the specific cell death inhibitors were added to the wells. To inhibit apoptosis, 10 μM of z-Vad-FMK (780051, Bachem AG) was used, for necroptosis, 10 μM of Necrostatin-S1 (17802, Cell Signalling Technology) and for ferroptosis, 1 μM of Ferrostatin-1 (SML0583, Sigma-Aldrich) was used. This was incubated for 4 h at 37 °C, after which the cells were treated with the high NTP treatment energy. After 24 h of incubation at 37 °C, fluorescence was measured and analyzed using the Spark® Cyto (Tecan, Switzerland). To determine cell death per area, the sum of the green fluorescence, corresponding to the amount of dead cells, was divided by the confluence.

Apoptosis analysis

To look further into apoptosis, caspase-3/7 activity was measured using the Incucyte Caspase-3/7 Green Dye for Apoptosis (4440, Sartorius). The parental and resistant A375 cells were treated with the low and high NTP treatment energies and incubated at 37 °C. After 22 h, the cell culture medium was removed and replaced with fresh medium containing 200 mM Hoechst 33342 (ThermoFischer, 62249) and 5 μM Incucyte Caspase-3/7 Green reagent. After 2 h of incubation at 37 °C, fluorescence was measured and analyzed using the Spark® Cyto (Tecan, Switzerland). To determine the percentage of caspase-3/7 positive cells, the green object count, corresponding to the caspase-3/7 positive cells was divided by the blue object count, corresponding to the total amount of cells in the well: $Caspace3/7Positivity(\%) = \frac{Caspase\ positive\ cell\ count}{total\ cells}$. Caspase 3/7 positivity was then normalized to the untreated of each condition (A375 or A375-NTP-R) and represented as fold change.

Incucyte® Annexin V Dye for Apoptosis (4641, Sartorius) was added to each well (1:200 dilution) in order to measure membrane-bound phosphatidylserine. Cells were incubated for 24 h at 37 °C and then imaged with the Incucyte® ZOOM live-cell imager (Sartorius, Germany). Analysis performed on the Incucyte software v2018A and Annexin V positivity was normalized to cell confluence per treatment condition: $Annexin\ V\ Positivity = \frac{AnnexinV\ positive\ cell\ count}{cell\ confluence}$. Annexin V positivity was then normalized to the untreated of each condition (A375 or A375-NTP-R) and represented as fold change.

Lipid peroxidation analysis

Oxidation of cellular lipids was measured using the Image-iT™ Lipid Peroxidation Kit (C10445, Invitrogen), according to the manufacturer's instructions. In short, the parental and resistant A375 cells were treated with the low and high NTP treatment energies and incubated for 24 h. The cells used for the positive controls were incubated with 100 μM cumene hydroperoxide for 1.5 h. After incubation, the C11-BODIPY dye was added to the wells with a final concentration of 10 μM and incubated for 30 min at 37 °C. The cells were washed twice with PBS and once with FACS buffer before acquisition was performed with the CytoFLEX (Beckman Coulter, USA). The ratios of the red over green mean fluorescence intensity signals were calculated using the FlowJo v10.8.1 (FlowJo LLC, USA).

Statistics

Statistical differences were calculated using JMP Pro 13 (SAS software, USA). All experiments were performed in triplicates with at least three independent replicates. The generalized linear mixed model was

used with treatment as fixed effect and the different independent replicates as random effects. When a significant difference was measured ($p \leq 0.05$), an adjusted p value was calculated based on multiple comparison tests, Dunnett's test when comparing to one group or Tukey's test when comparing all conditions to each other. All figures were prepared in GraphPad Prism (Dotmatics, UK) and the total number of observations (n) are represented as individual, while the mean ± SEM are also shown.

Acknowledgments

The authors would like to thank Dr. Christophe Deben and Ms. Hannah Zaryouh (Center for Oncological Research, University of Antwerp) for the use and their help with the D300e Digital Dispenser and Spark® Cyto, as well as Ms. Raphaëlle Corremans (Laboratory Pathophysiology, University of Antwerp) for the use of their lactate meter. The authors would also like to acknowledge the help from Ms. Tias Verhezen and Mr. Cyrus Akbari, who was involved at the start of the project but could not continue due to the COVID-19 pandemic. The authors also acknowledge the resources and services provided by the VSC (Flemish Supercomputer Center). This work was funded in part by the Research Foundation - Flanders (FWO) and the Flemish Government. The FWO fellowships and grants that funded this work also include: 12S9221N (Abraham Lin), G044420N (Abraham Lin, Annemie Bogaerts), and 1S67621N (Hanne Verswyvel). We would also like to thank several patrons, as part of this research was funded by donations from different donors, including Dedert Schilde vzw, Mr. Willy Floren, and the Vereycken family. We would also like to acknowledge the support from the European Cooperation in Science & Technology (COST) Action on "Therapeutical applications of Cold Plasmas" (CA20114; PlasTHER). Figs. 1 and 6 was created in part with BioRender.com.

Appendix A. Supporting information

Supplementary data associated with this article can be found in the online version at doi:10.1016/j.drup.2022.100914.

References

Avram, S., et al., 2017. Standardization of A375 human melanoma models on chicken embryo chorioallantoic membrane and Balb/c nude mice. Oncol. Rep. 38, 89–99.
Baghban, R., et al., 2020. Tumor microenvironment complexity and therapeutic implications at a glance. Cell Commun. Signal. 18, 1–19.
Barsoum, I.B., Smallwood, C.A., Siemens, D.R., Graham, C.H., 2014. A mechanism of hypoxia-mediated escape from adaptive immunity in cancer cells. Cancer Res. 74, 665–674.
Bartrons, R., Caro, J., 2007. Hypoxia, glucose metabolism and the Warburg's effect. J. Bioenerg. Biomembr. 39, 223–229.
Bekeschus, S., et al., 2017. Oxygen atoms are critical in rendering THP-1 leukaemia cells susceptible to cold physical plasma-induced apoptosis. Sci. Rep. 7, 1–12.
Bekeschus, S., et al., 2020. Medical gas plasma jet technology targets murine melanoma in an immunogenic fashion. Adv. Sci. 7, 1903438.
Bekeschus, S., et al., 2021. Tumor cell metabolism correlates with resistance to gas plasma treatment: the evaluation of three dogmas. Free Radic. Biol. Med. 167, 12–28.
Belisario, D.C., et al., 2020. Hypoxia dictates metabolic rewiring of tumors: implications for chemoresistance. Cells 9, 2598.
Bi, L., et al., 2021. HDAC11 regulates glycolysis through the LKB1/AMPK signaling pathway to maintain hepatocellular carcinoma stemness. Cancer Res. 81, 2015–2028.
Biscop, E., et al., 2019. The influence of cell type and culture medium on determining cancer selectivity of cold atmospheric plasma treatment. Cancers 11, 1287.
Bonzanini, A.D., Shao, K., Stancampiano, A., Graves, D.B., Mesbah, A., 2021. Perspectives on machine learning-assisted plasma medicine: towards automated plasma treatment. IEEE Trans. Radiat. Plasma Med. Sci.
Brand, A., et al., 2016. LDHA-associated lactic acid production blunts tumor immunosurveillance by T and NK cells. Cell Metab. 24, 657–671.
Chen, G., et al., 2020. Transdermal cold atmospheric plasma-mediated immune checkpoint blockade therapy. Proc. Natl. Acad. Sci. 117, 3687–3692.
Clemen, R., Heirman, P., Lin, A., Bogaerts, A., Bekeschus, S., 2020. Physical plasma-treated skin cancer cells amplify tumor cytotoxicity of human natural killer (NK) cells. Cancers 12, 3575.
Comerford, K.M., et al., 2002. Hypoxia-inducible factor-1-dependent regulation of the multidrug resistance (MDR1) gene. Cancer Res. 62, 3387–3394.
De Backer, J., et al., 2022. Cytoglobin silencing promotes melanoma malignancy but sensitizes for ferroptosis and pyroptosis therapy response. Antioxidants 11, 1548.
Ding, X.-c, et al., 2021. The relationship between expression of PD-L1 and HIF-1α in glioma cells under hypoxia. J. Hematol. Oncol. 14, 1–5.
Dobin, A., et al., 2013. STAR: ultrafast universal RNA-seq aligner. Bioinformatics 29, 15–21.
Dubuc, A., et al., 2018. Use of cold-atmospheric plasma in oncology: a concise systematic review, 1758835918786475 Ther. Adv. Med. Oncol. 10, 1758835918786475.
Efimova, I., et al., 2020. Vaccination with early ferroptotic cancer cells induces efficient antitumor immunity. J. Immunother. Cancer 8.
Elia, I., et al., 2022. Tumor cells dictate anti-tumor immune responses by altering pyruvate utilization and succinate signaling in CD8+ T cells. e1136 Cell Metab. 34, 1137–1150. e1136.
Fan, X.-D., Wan, L.-L., Duan, M., Lu, S., 2018. HDAC11 deletion reduces fructose-induced cardiac dyslipidemia, apoptosis and inflammation by attenuating oxidative stress injury. Biochem. Biophys. Res. Commun. 503, 444–451.
Franken, N.A., Rodermond, H.M., Stap, J., Haveman, J., Van Bree, C., 2006. Clonogenic assay of cells in vitro. Nat. Protoc. 1, 2315–2319.
Freund, E., et al., 2020. Risk evaluation of emt and inflammation in metastatic pancreatic cancer cells following plasma treatment. Front. Phys. 8, 569618.
Friedman, P., Miller, V., Fridman, G., Lin, A., Fridman, A., 2017. Successful treatment of actinic keratosis using non-thermal atmospheric pressure plasma- a case series. J. Am. Acad. Dermatol. 76, 352–353.
Friedmann Angeli, J.P., Krysko, D.V., Conrad, M., 2019. Ferroptosis at the crossroads of cancer-acquired drug resistance and immune evasion. Nat. Rev. Cancer 19, 405–414.
Georgescu, N., Lupu, A.R., 2010. Tumoral and normal cells treatment with high-voltage pulsed cold atmospheric plasma jets. IEEE Trans. Plasma Sci. 38, 1949–1955.
Guerrero-Preston, R., et al., 2014. Cold atmospheric plasma treatment selectively targets head and neck squamous cell carcinoma cells. Int. J. Mol. Med 34, 941–946.
Han, S.J., Kwon, S., Kim, K.S., 2021. Challenges of applying multicellular tumor spheroids in preclinical phase. Cancer Cell Int. 21, 1–19.
Hangauer, M.J., et al., 2017. Drug-tolerant persister cancer cells are vulnerable to GPX4 inhibition. Nature 551, 247–250.
Hassannia, B., Vandenabeele, P., Berghe, T.V., 2019. Targeting ferroptosis to iron out cancer. Cancer Cell 35, 830–849.
Hurtado, E., et al., 2021. HDAC11 is a novel regulator of fatty acid oxidative metabolism in skeletal muscle. FEBS J. 288, 902–919.
Icard, P., et al., 2018. How the Warburg effect supports aggressiveness and drug resistance of cancer cells? Drug Resist. Updates 38, 1–11.
Kanehisa, M., Goto, S., 2000. KEGG: kyoto encyclopedia of genes and genomes. Nucleic Acids Res. 28, 27–30.
Keidar, M., Yan, D., Beilis, I.I., Trink, B., Sherman, J.H., 2018. Plasmas for treating cancer: opportunities for adaptive and self-adaptive approaches. Trends Biotechnol. 36, 586–593.
Khalili, M., et al., 2019. Non-thermal plasma-induced immunogenic cell death in cancer. J. Phys. D: Appl. Phys. 52, 423001.
Kopecka, J., et al., 2021. Hypoxia as a driver of resistance to immunotherapy. Drug Resist. Updates, 100787.
Lee, J., You, J.H., Kim, M.-S., Roh, J.-L., 2020. Epigenetic reprogramming of epithelial-mesenchymal transition promotes ferroptosis of head and neck cancer. Redox Biol. 37, 101697.
Li, B., et al., 2020. Emerging mechanisms and applications of ferroptosis in the treatment of resistant cancers. Biomed. Pharmacother. 130, 110710.
Liberzon, A., et al., 2015. The molecular signatures database hallmark gene set collection. Cell Syst. 1, 417–425.
Lin, A., et al., 2017. Nanosecond-pulsed DBD plasma-generated reactive oxygen species trigger immunogenic cell death in A549 lung carcinoma cells through intracellular oxidative stress. Int. J. Mol. Sci. 18, 966.
Lin, A., et al., 2019. Non-Thermal plasma as a unique delivery system of short-lived reactive oxygen and nitrogen species for immunogenic cell death in melanoma cells. Adv. Sci. 6, 1802062.
Lin, A., et al., 2021a. Oxidation of innate immune checkpoint CD47 on cancer cells with non-thermal plasma. Cancers 13, 579.
Lin, A., et al., 2022. The effect of local non-thermal plasma therapy on the cancer-immunity cycle in a melanoma mouse model. Bioeng. Transl. Med., e10314
Lin, A., Biscop, E., Gorbanev, Y., Smits, E., Bogaerts, A., 2021b. Toward defining plasma treatment dose: the role of plasma treatment energy of pulsed-dielectric barrier discharge in dictating in vitro biological responses. Plasma Process Polym., e2100151
Liu, Q., et al., 2016. The CXCL8-CXCR1/2 pathways in cancer. Cytokine Growth Factor Rev. 31, 61–71.
Mahdikia, H., et al., 2021. Gas plasma irradiation of breast cancers promotes immunogenicity, tumor reduction, and an abscopal effect in vivo. OncoImmunology 10, 1859731.
Metelmann, H.-R., et al., 2018. Clinical experience with cold plasma in the treatment of locally advanced head and neck cancer. Clin. Plasma Med. 9, 6–13.
Privat-Maldonado, A., et al., 2022. Cold atmospheric plasma does not affect stellate cells phenotype in pancreatic cancer tissue in Ovo. Int. J. Mol. Sci. 23, 1954.
Raudvere, U., et al., 2019. g: Profiler: a web server for functional enrichment analysis and conversions of gene lists (2019 update). Nucleic Acids Res 47, W191–W198.
Rohwer, N., Cramer, T., 2011. Hypoxia-mediated drug resistance: novel insights on the functional interaction of HIFs and cell death pathways. Drug Resist. Updates 14, 191–201.
Scharping, N.E., Menk, A.V., Whetstone, R.D., Zeng, X., Delgoffe, G.M., 2017. Efficacy of PD-1 blockade is potentiated by metformin-induced reduction of tumor

hypoxiametformin improves PD-1 blockade immunotherapy. Cancer Immunol. Res. 5, 9–16.
Seto, E., Yoshida, M., 2014. Erasers of histone acetylation: the histone deacetylase enzymes. Cold Spring Harb. Perspect. Biol. 6, a018713.
Shoval, H., et al., 2017. Tumor cells and their crosstalk with endothelial cells in 3D spheroids. Sci. Rep. 7, 1–11.
Subramanian, A., et al., 2005. Gene set enrichment analysis: a knowledge-based approach for interpreting genome-wide expression profiles. Proc. Natl. Acad. Sci. 102, 15545–15550.
Tanaka, H., et al., 2017. State of the art in medical applications using non-thermal atmospheric pressure plasma. Rev. Mod. Plasma Phys. 1, 1–89.
Tanaka, H., et al., 2021. Plasma-treated solutions (pts) in cancer therapy. Cancers 13, 1737.
Tsang, S.M., Oliemuller, E. & Howard, B.A. in Semin. Cancer Biol. 3–11 (Elsevier).
Um, J.H., et al., 2004. Association of DNA-dependent protein kinase with hypoxia inducible factor-1 and its implication in resistance to anticancer drugs in hypoxic tumor cells. Exp. Mol. Med. 36, 233–242.
Van der Paal, J., Neyts, E.C., Verlackt, C.C., Bogaerts, A., 2016. Effect of lipid peroxidation on membrane permeability of cancer and normal cells subjected to oxidative stress. Chem. Sci. 7, 489–498.
Van der Paal, J., Verheyen, C., Neyts, E.C., Bogaerts, A., 2017. Hampering effect of cholesterol on the permeation of reactive oxygen species through phospholipids bilayer: possible explanation for plasma cancer selectivity. Sci. Rep. 7, 1–11.
Van Loenhout, J., et al., 2019. Cold atmospheric plasma-treated PBS eliminates immunosuppressive pancreatic stellate cells and induces immunogenic cell death of pancreatic cancer cells. Cancers 11, 1597.
Van Loenhout, J., et al., 2021. Auranofin and cold atmospheric plasma synergize to trigger distinct cell death mechanisms and immunogenic responses in glioblastoma. Cells 10, 2936.
Vara-Pérez, M., et al., 2021. BNIP3 promotes HIF-1α-driven melanoma growth by curbing intracellular iron homeostasis. EMBO J. 40, e106214.
Viswanathan, V.S., et al., 2017. Dependency of a therapy-resistant state of cancer cells on a lipid peroxidase pathway. Nature 547, 453–457.
Wang, H., Jiang, H., Van De Gucht, M., De Ridder, M., 2019. Hypoxic radioresistance: can ROS be the key to overcome it? Cancers 11, 112.
Wende, K., von Woedtke, T., Weltmann, K.-D., Bekeschus, S., 2019. Chemistry and biochemistry of cold physical plasma derived reactive species in liquids. Biol. Chem. 400, 19–38.
Wrann, S., Kaufmann, M.R., Wirthner, R., Stiehl, D.P., Wenger, R.H., 2013. HIF mediated and DNA damage independent histone H2AX phosphorylation in chronic hypoxia. Biol. Chem. 394, 519–528.
Xu, T., et al., 2019. Molecular mechanisms of ferroptosis and its role in cancer therapy. J. Cell. Mol. Med. 23, 4900–4912.
Yadav, U.P., et al., 2020. Metabolic adaptations in cancer stem cells. Front. Oncol. 10, 1010.
Yan, D., et al., 2015. Toward understanding the selective anticancer capacity of cold atmospheric plasma—A model based on aquaporins. Biointerphases 10, 040801.
Yusupov, M., et al., 2021. Oxidative damage to hyaluronan–CD44 interactions as an underlying mechanism of action of oxidative stress-inducing cancer therapy. Redox Biol. 43, 101968.
Zucker, S.N., et al., 2012. Preferential induction of apoptotic cell death in melanoma cells as compared with normal keratinocytes using a non-thermal plasma torch. Cancer Biol. Ther. 13, 1299–1306.